PRICING PLAIN VANILLA OPTIONS ON HENRY HUB FUTURES: INTRODUCING A HUMP-SHAPED VOLATILITY MODEL

Luis Berruguete Ascanio

Trabajo de investigación 25/009

Master en Banca y Finanzas Cuantitativas

Tutoras: Dra. M. Carmen Frau
Dra. M. Dolores Robles

Universidad Complutense de Madrid

Universidad del País Vasco

Universidad de Valencia

Universidad de Castilla-La Mancha

www.finanzascuantitativas.com

UNIVERSIDAD COMPLUTENSE DE MADRID

Facultad de Ciencias Económicas y Empresariales

MASTER'S IN QUANTITATIVE FINANCE AND BANKING

MASTER'S THESIS

Pricing Plain Vanilla Options on Henry Hub Futures: Introducing a Hump-Shaped Volatility Model

Luis Berruguete

Supervisors

M. CARME FRAU (UIB)

M. DOLORES ROBLES (UCM)

Course 2024-2025

Abstract:

In this work, we develop a new term-structure model for commodity futures prices, we propose a novel specification of the volatility function aimed to provide a hump-shaped pattern in the mid-tenor region of the variance curve. This distinctive empirical regularity is observed in natural gas markets. The model retains the log-normal dynamics of futures prices, which allows the finding of closed-form formulas for option pricing. Furthermore, we derive analytical expressions for the main Greeks. The performance of our model is evaluated against two widely used benchmarks in the literature. An in-sample test and our analysis of Greeks-based approximation of options prices, demonstrate that our model outperforms the established benchmarks for pricing European plain vanilla options on Henry Hub natural gas futures, providing superior pricing accuracy.

Keywords:

Henry Hub, commodities, humps, futures, European plain vanilla options, volatility modeling, analytic expressions, Greeks.

Contents

1 Introduction

The valuation of derivative instruments on commodities is a central topic in financial economics, both for its theoretical interest and its practical relevance in risk management and trading. The present study examines the pricing of European plain vanilla options (options hereafter) on natural gas futures. Within commodity markets, natural gas plays a particularly significant role due to its importance in the energy sector and the economy, it fuels power plants to generate electricity and is widely used for domestic cooking and heating. We select the American natural gas Henry Hub (HH hereafter) futures as it provides the most liquid venue for natural gas trading, which serves as the benchmark for the North American gas derivative market. HH futures and options are highly liquid and observable, enabling direct calibration to market-implied volatilities across a wide spectrum of strikes and maturities.

There are two main streams in the literature on commodity option pricing. The first adopts a spot price-based framework (i.e., Gibson & Schwartz (1990), Schwartz (1997), Geman (2000), Schwartz & Smith (2000), Lucía & Schwartz (2002), Casassus & Collin-Dufresne (2005)), and the second one uses the evolution of the futures curve (i.e., Black (1976), Clewlow & Strickland (1999a,b), Crosby (2008), Trolle & Schwartz (2009), Crosby & Frau (2022), Frau & Fanelli (2023)). Some models incorporate jump dynamics, others introduce stochastic volatility, still others seasonality effects, and few of them combine two or more of these features within a single framework. In this work, we adopt a futures-based modeling framework for several reasons. Spot price-based approaches require the estimation of unobservable components, such as the convenience yield or storage costs, in addition to the practical difficulty of obtaining reliable spot prices. Conversely, a futures-based approach ensures an arbitrage-free term-structure by design: under the risk-neutral measure, the drift of the future price is zero. The dynamics are fully characterized through the volatility specification, which eliminates the need to impose potentially misspecified drift conditions or to adjust for convenience-yield processes that may not map directly to observable prices. By modeling the volatility to capture these features directly in the futures-curve dynamics, we maintain tractability and guarantee consistency across the entire curve.

The Samuelson effect is commonly assumed as a universal feature of commodity futures markets: volatility is expected to decline monotonically with TTM. However, our analysis indicates that natural gas markets frequently exhibit an alternative pattern, a hump-shaped term structure of option implied volatilities: short-dated contracts exhibit elevated volatility, which declines as TTM increases, and subsequently rises again at intermediate maturities. This feature is illustrated by Figure 1, which shows the calibrated market-implied volatilities grouped by each HH generic futures contract. This systematic behavior motivates the need to develop new models specifically designed to capture such dynamics, extending beyond the purely exponential decay of traditional benchmarks.

The present study contributes to this line of research by proposing a new term-structure

model for natural gas futures prices, which we call **CS+H**. Based on the model Clewlow & Strickland (1999b), we propose a novel specification of the volatility function aimed to provide a hump-shaped pattern in the mid-tenor region of the variance curve. This hump feature adds theoretical flexibility to the model and allows to capture this empirically observed fact in natural gas markets. In addition, the model retains the log-normal dynamics of futures prices, which allows the finding of closed-form formulas for option pricing. Furthermore, we derive the main Greeks of the model, which provide analytical sensitivities useful for both option pricing and for risk management applications. To the best of our knowledge, our is the first deterministic volatility specification with a hump component proposed for natural gas markets. There is an extensive literature on stochastic volatility models in different commodities (i.e., Trolle & Schwartz (2009), Schneider & Tavin (2018, 2021)), including hump-shaped stochastic volatility specifications for crude oil markets (i.e., Chiarella et al. (2013), Cheng et al. (2018), Kang et al. (2020)). However, there are deterministic hump-shaped volatility functions developed for interest rate term-structure modeling (i.e., the power-exponential models proposed by Moraleda & Vorst (1997), Mercurio & Moraleda (2000)).

To assess the practical significance of the hump-shaped volatility model proposed, we compare its performance along with other two futures-based models: i) Black (1976) (hereafter **Bla76**), the classic log-normal one-factor model with constant volatility. We adopt this model due to its closed-form tractability, single-parameter calibration, and widespread acceptance as the industry standard[1]; ii) Clewlow & Strickland (1999b) (hereafter **CS99b**), an affine futures-curve model incorporating the Samuelson effect via a volatility term that exponentially decays with TTM.

We obtain closed-form formulas for option pricing, and derive analytical expressions for the main Greeks. Furthermore, we conduct an extensive empirical analysis of these models. First, we evaluate the performance both in-sample and out-of-sample. In the in-sample analysis, special attention is devoted to subperiods marked by unexpected shocks, such as extreme weather events, supply disruptions, or geopolitical tensions that directly or indirectly affect US natural gas prices. By comparing these two distinct analysis frameworks, stable vs stress periods, we identify which model delivers the most robust empirical performance under varying market conditions. Second, we present a novel approximation method based on the Greeks of the models. This approach provides insight into the explanatory power of first and second order sensitivities under relatively stable market conditions, while also allowing us to detect potential deviations associated with more abrupt events, such as jumps or spikes. Our results demonstrate that CS+H improves pricing accuracy relative to the benchmarks. The model consistently outperforms Bla76 and delivers measurable gains over CS99b, particularly when calibration is performed with more granularity. These improvements are most evident during periods of market stress, when volatility term-structures deviate from monotonic patterns and the additional flexibility of

[1]This model is the industry standard for quoting implied volatilities for options on commodities when prices are quoted in the form of futures.

CS+H allows the model to capture the observed dynamics more faithfully.

The thesis is organized as follows. Section 2 presents the theoretical framework, contextualizing the definition of commodities, the particular features of natural gas, and the functioning of commodity markets. Section 3 introduces and describes the CS+H model; Section 4 derives the main Greeks of our model. Section 5 describes the basic characteristics of the data set used in the empirical study. Section 6 details the calibration and validation methodology employed for each model. Section 7 reports the empirical results obtained from its implementation. Section 8 presents a novel approximation method based on the Greeks of our model. Finally, Section 9 summarizes the principal conclusions.

2 Commodity Market Context

A commodity is a standardized, fungible good or raw material attributable to a natural resource that is traded on organized markets, such as the New York Mercantile Exchange (NYMEX, part of the CME Group) and the Intercontinental Exchange (ICE), among others. Commodities span multiple sectors, including precious metals (such as gold or silver), industrial metals (such as aluminum or copper), livestock (such as live cattle or feeder pigs), agricultural products (such as wheat or corn), and energy resources (such as crude oil or natural gas). Natural gas, in particular, serves as a major fuel for power plants for electricity generation, industrial processes, and domestic heating.

According to Energy Institute (2025), the world's leading natural gas producers in 2024 are the US, Russia, Iran, China, Canada, Qatar, and Australia. These seven countries together accounted for around 65% of global natural gas production. Individually, the US was responsible for about 25% and Russia for 15%, underscoring their dominant position in the global natural gas market. The exportation of countries' surplus is made either via cross-border pipelines or as liquefied natural gas (LNG).[2] Before the advent of LNG, gas markets were confined to regional pipeline networks. Today, a truly global natural gas market is emerging, linking every production center with the major demand centers all over the globe.

North America, which comprises the US, Canada, and Mexico, hosts a large number of trading hubs. The HH, located in southern Louisiana (US), functions as the principal delivery point for natural gas futures contracts traded on NYMEX. It is strategically situated in a major onshore production region and is also close to offshore production, so multiple pipelines from producing basins converge at this hub. For these reasons, the HH emerges as the widely accepted benchmark for North American natural gas. In Western Europe, the most important hub is the Title Transfer Facility (TTF) in the Netherlands. The Japan Korea Marker (JKM) has gained prominence as the benchmark for LNG trade in Asia.

Futures contracts allow market participants to hedge or speculate on anticipated price move-

[2]LNG is cooled to about –160 °C (–260°F) so it can be shipped in refrigerated tankers and then regasified at its destination for delivery through standard pipelines.

ments, reflecting collective expectations about future supply, demand, and logistic factors, among others. Actual supply and demand conditions determine the physical spot price, whereas futures prices incorporate a risk-neutral expectation of these dynamics over the life of the contract. The HH market is one of the most liquid venues for trading natural gas futures and options worldwide. According to CME Group (2025), each HH futures contract represents 10,000 million British thermal units (MMBtu) of deliverable natural gas with a minimum tick price of $0.001 per MMBtu. They trade electronically six days a week, 23 hours per day (with a daily 60-minute break at 5 p.m. ET), and carry monthly expirations extending several years into the future; trading activity concentrates primarily in the front six to nine delivery months.

2.1 Established Stylized Facts in Natural Gas Markets

Natural gas prices, whether spot or futures, exhibit several well-documented empirical features, such as seasonality, mean-reversion, and the Samuelson effect.

Seasonality in prices is primarily driven by increased demand during the winter months, due to heating needs. As a result, futures curves display a pronounced sinusoidal pattern: contract prices for delivery during high-demand months (typically November through March) tend to trade at a relative premium compared to low-demand months (typically April through October), as illustrated in Figure 2.

In addition, natural gas prices generally revert to a long-term mean value: short-lived supply shocks or weather events can cause prices to deviate temporarily, but over time, the price drifts back toward equilibrium, as shown in Figure 3. This figure displays the evolution of natural gas futures prices for contracts HHc2, HHc4, and HHc6 over our sample period. Futures prices exhibit pronounced spikes during 2021–2022, followed by a gradual decline and stabilization around lower levels.

Finally, the Samuelson effect refers to the empirical observation that the volatility of futures contracts increases as the contract approaches expiration. Nearer-month contracts are more sensitive to short-term supply or demand imbalances and thus exhibit higher instantaneous volatility; in contrast, long-dated contracts display a dampened volatility profile as seen in Figure 4. This figure is constructed by averaging the market-implied option volatilities across the HH generic futures contracts HHc1 through HHc9 on January 17, 2025.[3]

2.2 The Samuelson Effect and Its Limitations

Although the Samuelson effect is commonly assumed to be universal across commodity markets, our analysis reveals that both the Samuelson effect and the hump-shaped behavior can be observed in practice. As Figure 4 illustrates, there are dates (e.g., January 17, 2025) when the term-structure of option implied volatilities declines monotonically with maturity, consistent

[3]See Section 5 for additional information on HH generic contracts.

with the Samuelson effect. On other dates (e.g., January 29, 2025), the term-structure departs from monotonicity and a hump-shaped term-structure emerges, as plotted in Figure 5. Moreover, when option implied volatilities are obtained from a "grouped-by-contract" calibration[4] using Bla76, as displayed in Figure 1, this hump-shaped pattern supersedes the Samuelson effect. To assess the prevalence of both dynamics, we analyze our full panel of trading days $1,252$: in 666 (53.2%) cases the Samuelson effect holds, whereas in 586 (46.8%) cases it does not. This coexistence motivates the need for a modeling framework flexible enough to capture either behaviors.

3 From CS99b to CS+H: Modeling a Term-Structure for the Volatility with Humps

In this section we introduce our proposed deterministic volatility model, denoted as CS+H. This futures-curve model incorporates the Samuelson effect via a volatility term that decays exponentially with TTM, while also allowing for a hump-shaped pattern in the mid-tenor region of the variance curve. The motivation for this specification arises directly from empirical evidence, the aforementioned "grouped-by-contract" calibrated term-structure is non–monotonic: volatility is high for short maturities, declines as TTM increases, but rises at intermediate maturities creating the hump shape. Figure 1 illustrates this feature, showing market-implied option volatilities under the Bla76 specification, grouped per HH generic futures contract. From observed market prices of call options, we compute the corresponding implied volatilities by numerically inverting Black's formula via the bisection method.[5]

In the remainder of this section, we specify the risk-neutral dynamics of the futures price SDE, the implied spot price SDE, and obtain the expression for the futures price $F(t,T)$. We then verify that $F(t,T)$ satisfies the martingale condition under the risk-neutral measure Q and compute the conditional distribution of $F(T,T)$, demonstrating its log-normality. By exploiting this result, we obtain closed-form formulas for option pricing.

As previously discussed, the CS+H model represents an extension of the CS99b framework, which is itself an extension of the classical Bla76 model. The CS+H specification nests both Bla76 and CS99b as special cases, providing a unified structure that facilitates consistent comparison across modeling approaches. A comparative summary of the model dynamics and integrated variances between Bla76, CS99b, and CS+H is provided in Table 1.

[4]This procedure yields one implied volatility per contract. See Section 3 for details.

[5]At each step we set $\sigma_{\text{mid}} = (\sigma_{\text{min}} + \sigma_{\text{max}})/2$, evaluate $f(\sigma_{\text{mid}})$, and replace the bound whose f-value has the same sign as $f(\sigma_{\text{mid}})$ by σ_{mid}, thereby keeping the root bracketed. We repeat this until $\sigma_{\text{max}} - \sigma_{\text{min}}$ is below our tolerance, and take $\sigma = (\sigma_{\text{min}} + \sigma_{\text{max}})/2$ as the implied volatility.

3.1 Model Dynamics

We propose a one-factor extension of the CS99b model by enriching the volatility term-structure with an additional parameter κ that allows capturing hump-shaped volatilities. In this framework, the futures-price dynamics under the risk-neutral measure is

$$\frac{dF(t,T)}{F(t,T)} = \big(\sigma + \kappa(T-t)\big)\, e^{-\alpha(T-t)}\, dW_t. \tag{3.1}$$

The model in equation (3.1) has three volatility parameters: $\sigma > 0$ is the base volatility level, $\alpha > 0$ controls the exponential decay rate of volatility for long maturities, and the new parameter $\kappa > 0$ introduces a linear tilt that produces a pronounced hump in the mid-tenor region. Additionally, dW_t denotes a Wiener process.

Any specification of the whole futures price dynamics implies a process for the spot price. For the specification in Equation (3.1), the implied spot price process is

$$\begin{aligned}
\frac{\mathrm{d}S(t)}{S(t)} = & \underbrace{\left(\frac{\partial}{\partial t}\ln F(0,t) + \alpha\big(\ln F(0,t) - \ln S(t)\big) + \tfrac{\sigma^2}{4}\big(1 - M(0,t)\big)\right) dt + \sigma\,\mathrm{d}W_t}_{\text{CS99b}} \\
& + \left(\frac{1}{2\alpha}\left(-(\sigma\kappa - \alpha\sigma^2)(1-M(0,t)) - (\kappa^2 - 2\alpha\sigma\kappa)\left(-tM(0,t) + \frac{1-M(0,t)}{2\alpha}\right)\right.\right. \\
& \left. - \alpha\kappa^2\left(-t^2 M(0,t) - \frac{t}{\alpha}\,M(0,t) + \frac{1-M(0,t)}{2\alpha^2}\right)\right) \\
& \left. + (\kappa - \alpha)\left(\ln S(t) - \ln F(0,t) + \frac{V^2(0,t)}{2}\right)\right) dt,
\end{aligned} \tag{3.2}$$

with $V^2(0,t) = A\big(1 - M(0,t)\big) - B(0,t)\,M(0,t)$, where

$$A = \frac{1}{2\alpha}\left(\sigma^2 + \frac{\sigma\kappa}{\alpha} + \frac{\kappa^2}{2\alpha^2}\right), \quad B(0,t) = \frac{\kappa(t-0)}{\alpha}\left(\sigma + \frac{\kappa(t-0)}{2} + \frac{\kappa}{2\alpha}\right), \quad M(0,t) = e^{-2\alpha(t-0)}.$$

And the futures curve reads

$$\begin{aligned}
F(t,T) = F(0,T)\,\exp & \underbrace{\left\{\sqrt{M(t,T)}\ln\!\left(\frac{S(t)}{F(0,t)}\right) - \tfrac{\sigma^2}{4\alpha}\sqrt{M(0,T)}\big(e^{2\alpha t} - 1\big)\big(\sqrt{M(0,T)} - \sqrt{M(0,t)}\big)\right\}}_{\text{CS99b}} \\
& \times \exp\left\{\sqrt{M(t,T)}\,\kappa(T-t)\int_0^t \sqrt{M(u,t)}\,\mathrm{d}W_u + \tfrac{1}{2}\big(\sqrt{M(t,T)} - 1\big)\,V^2(0,t)\right\}.
\end{aligned}$$

These expressions highlight how the presence of κ produces a non-monotonic hump-shaped volatility curve. This feature allows the model to capture peaks in the medium-term natural gas futures. The steps followed to get to these expressions can be found in Appendix B.

3.2 Futures Price Derivation

We define the futures price under the risk-neutral measure Q by

$$F(t,T) \;=\; \mathbb{E}_t^Q\big[F(T,T)\big] = \;\mathbb{E}_t^Q\big[S(T)\big].$$

Applying Itô's lemma to the process $f(t) = \ln F(t,T)$, note that

$$d\big[\ln F(t,T)\big] = \frac{1}{F(t,T)}\,dF(t,T) - \frac{1}{2}\,\frac{1}{F(t,T)^2}\,\big(dF(t,T)\big)^2.$$

Under the model specification in (3.1), applying Itô's lemma and integrating from t to T we have

$$\begin{aligned}\ln F(T,T) - \ln F(t,T) = -\tfrac{1}{2}\int_t^T M(s,T)\big(\sigma^2 + 2\,\sigma\,\kappa\,(T-s) + \kappa^2\,(T-s)^2\big)\,\mathrm{d}s \\ + \int_t^T \big(\sigma + \kappa\,(T-s)\big)\sqrt{M(s,T)}\,\mathrm{d}W_s. \qquad (3.3)\end{aligned}$$

Taking conditional expectation $\mathbb{E}_t^Q[\cdot]$, and given that $\ln F(t,T)$ is $\mathscr{F}_t$-measurable and the Itô integral has zero mean, we obtain

$$\mathbb{E}_t^Q\big[\ln F(T,T)\big] = \ln F(t,T) - \underbrace{\tfrac{1}{2}\int_t^T M(s,T)\big(\sigma^2 + 2\,\sigma\,\kappa\,(T-s) + \kappa^2\,(T-s)^2\big)\,\mathrm{d}s}_{V^2(t,T)}.$$

We denote the integral above by

$$V^2(t,T) \equiv A\big(1 - M(t,T)\big) \;-\; B(t,T)\,M(t,T),$$

with functions A, B, M as in (3.2) evaluated over the interval (t,T). Hereafter, we denote $V^2 \equiv V^2(t,T)$, $B \equiv B(t,T)$, $M \equiv M(t,T)$; we make this simplification since these variables are not referenced over the interval $(0,t)$ anymore. Then,

$$\mathbb{E}_t^Q\big[\ln F(T,T)\big] = \ln F(t,T) - \tfrac{1}{2}\big(A(1-M) - BM\big).$$

The only random term in (3.3) is the stochastic integral, its conditional variance $\mathbb{V}_t^Q[\cdot]$ is

$$V^2 \equiv \mathbb{V}_t^Q\big[\ln F(T,T)\big] = \mathbb{V}_t^Q\Big[\int_t^T \big(\sigma + \kappa\,(T-s)\big)\,\sqrt{M(s,T)}\,\mathrm{d}W_s\Big] = \int_t^T \big(\sigma + \kappa\,(T-s)\big)^2\,M(s,T)\,\mathrm{d}s.$$

We show that $F(t,T)$ is a Q-martingale by verifying

$$\mathbb{E}_t^Q\big[F(T,T)\big] = F(t,T). \qquad (3.4)$$

We have shown in the Appendix (B) that

$$\mathbb{E}_t^Q\big[F(T,T)\big] = F(t,T)\exp\big\{-\tfrac{1}{2}V^2+\tfrac{1}{2}V^2\big\} = F(t,T),$$

which completes the proof of (3.4)

$$F(t,T) \;=\; \mathbb{E}_t^Q\big[F(T,T)\big] \;=\; \mathbb{E}_t^Q\big[S(T)\big],$$

proving that $F(t,T)$ is a martingale.

3.3 Option Pricing

We begin by defining the time-t price of a call option $c(t)$ on a futures contract, with maturity T and strike K. Let T_0 denote the maturity of the option. Although in practice the European plain vanilla option on HH expires one business day before the associated futures contract, for analytical convenience, we treat both maturities as identical ($T_0 = T$).[6] Under the risk-neutral measure Q, we have

$$c(t) = e^{-r(T-t)}\,\mathbb{E}_t^Q\big[\max\{F(T,T)-K,0\}\big],$$

where r is the constant risk-free rate and $\mathbb{E}_t^Q[\cdot]$ denotes the conditional expectation given information at time t. From (3.3) we have

$$\begin{aligned}\ln F(T,T)-\ln F(t,T) = -\tfrac{1}{2}\int_t^T M(s,T)\big(\sigma^2+2\sigma\kappa(T-s)+\kappa^2(T-s)^2\big)\,\mathrm{d}s \\ +\int_t^T\big(\sigma+\kappa(T-s)\big)\sqrt{M(s,T)}\,\mathrm{d}W_s,\end{aligned}$$

that is, $\ln F(T,T)$ is normally distributed under Q: $\ln F(T,T)\sim\mathcal{N}\big(\mu,V^2\big)$, where

$$\mu = \ln F(t,T)-\tfrac{1}{2}V^2, \quad V^2 = A(1-M)-BM. \tag{3.5}$$

Formally, Black's option pricing formula on a futures contract is

$$c(t) = e^{-r(T-t)}\big(F(t,T)\,\mathcal{N}(d_1)\;-\;K\,\mathcal{N}(d_2)\big), \tag{3.6}$$

$$d_1 = \frac{\ln\big(F(t,T)/K\big)+\frac{1}{2}V^2}{V}, \qquad d_2 = d_1 - V.$$

Here V is the total volatility over $[t,T]$, $\mathcal{N}(x)$ and $\mathcal{N}'(x)$ denote the cumulative distribution function (CDF) of the standard normal law and its probability density function (PDF), respectively.[7] By substituting the model-specific form of V^2 into (3.6), we obtain an ex-

[6] This one-day difference between future and option maturities is negligible in our context, since we consider futures contracts with maturities ranging from one to nine months.

[7] $\mathcal{N}(x) = \frac{1}{\sqrt{2\pi}}\int_{-\infty}^{x} e^{-z^2/2}\,\mathrm{d}z$ and $\mathcal{N}'(x) = \frac{1}{\sqrt{2\pi}}\,e^{-x^2/2}$.

plicit analytic pricing expression for a call option under the CS+H framework.[8] Under the CS+H specification, we have that V^2 is given by (3.5). Notice that using the put–call parity, $p(t) = c(t) - e^{-r(T-t)}\big(F(t,T) - K\big)\big)$, we can obtain the put prices directly from the corresponding call prices with the same strike K and maturity T.

4 Greeks of a Call Option

In this section, we derive the analytical Greeks of a call option written on a futures contract, using equation (3.6). Notice that using the put–call parity, we can obtain the put Greeks directly from the corresponding call Greeks. Every derivation step for each Greek can be found in Appendix C.

4.1 Delta (Δ_c)

Delta measures the sensitivity of the call option's price $c(t)$ to infinitesimal changes in the underlying price $F(t,T)$. Its expression reads

$$\Delta_c = e^{-r(T-t)}\,\mathcal{N}\big(d_1\big).$$

Since $\mathcal{N}(d_1)$ is the CDF of a standard normal distribution, it follows that $0 < \Delta_c < 1$. In other words, Δ_c can be viewed as the discounted CDF of a $\mathcal{N}(0,1)$ under the risk-neutral measure Q. Consequently, if the futures price $F(t,T)$ increases by one unit, the call premium increases by exactly Δ_c units, which is always less than the full one-unit move in $F(t,T)$.

4.2 Gamma (Γ_c)

Gamma measures the sensitivity of the call options' Delta Δ_c to infinitesimal changes in the underlying price $F(t,T)$. It quantifies the convexity of the call premium with respect to $F(t,T)$, and thus the necessity to rebalance a hedged position. Its expression reads

$$\Gamma_c = \frac{e^{-r(T-t)}\,\mathcal{N}'\big(d_1\big)}{F(t,T)\,V}.$$

4.3 Vega (ν_c)

Vega measures the sensitivity of the price of a call option $c(t)$ with respect to the instantaneous volatility parameter V. In particular, under the CS+H specification, V itself depends on σ, α, and κ. In practice, we therefore define three separate parameter-Vegas:

$$\nu_c^{\sigma} = \frac{\partial c}{\partial \sigma} = \frac{\partial c}{\partial V}\frac{\partial V}{\partial \sigma}, \quad \nu_c^{\alpha} = \frac{\partial c}{\partial \alpha} = \frac{\partial c}{\partial V}\frac{\partial V}{\partial \alpha}, \quad \nu_c^{\kappa} = \frac{\partial c}{\partial \kappa} = \frac{\partial c}{\partial V}\frac{\partial V}{\partial \kappa}.$$

[8] Note that V^2 varies across models; the specific expressions are given in Table 1.

4.3.1 Sigma-Vega (ν_c^{σ})

Sigma-Vega measures how the option price reacts to changes in the short-term level of volatility. It reflects the local or baseline impact of instantaneous volatility shocks on the option premium. measures sensitivity to the base volatility level. Its expression reads

$$\nu_c^{\sigma} = \frac{\Lambda}{2V\alpha}\left(\left(\sigma + \frac{\kappa}{2\alpha}\right)(1-M) - \kappa(T-t)M\right), \tag{4.1}$$

with $\Lambda = e^{-r(T-t)}\, F(t,T)\, \mathcal{N}'(d_1)$.

4.3.2 Alpha-Vega (ν_c^{α})

Alpha-Vega captures the sensitivity to the exponential decay rate of volatility for longer maturities. An increase in $\alpha > 0$ causes faster decay in V, flattening the term-structure and reducing long-tenor volatility exposure. Its expression reads

$$\nu_c^{\alpha} = \frac{\Lambda}{2V\alpha^2}\left(\left(-\frac{\sigma^2}{2} - \frac{\sigma\kappa}{\alpha} - \frac{3\kappa^2}{4\alpha^2}\right)(1-M) + (T-t)\left(\kappa\left(\sigma + \frac{\kappa(T-t)}{2} + \frac{\kappa}{\alpha}\right) + 2\alpha^2(A+B)\right)M\right).$$

4.3.3 Kappa-Vega (ν_c^{κ})

Kappa-Vega quantifies sensitivity to the linear tilt parameter. As $\kappa > 0$ amplifies the hump effect in the mid-tenor region, this Vega reflects how changes in the curvature of the volatility term-structure influence the option price. Its expression reads

$$\nu_c^{\kappa} = \frac{\Lambda}{2V\alpha}\left(\left(\frac{\sigma}{2\alpha} + \frac{\kappa}{2\alpha^2}\right)(1-M) - (T-t)\left(\sigma + \kappa(T-t) + \frac{\kappa}{\alpha}\right)M\right).$$

4.4 Rho (ρ_c)

Rho of the call measures the sensitivity of its price $c(t)$ with respect to changes in the risk–free interest rate r. Its expression reads

$$\rho_c = -c(t)(T-t).$$

4.5 Theta (θ_c)

Theta of the call measures the sensitivity of its price $c(t)$ with respect to changes in the derivative's TTM. Its expression reads

$$\theta_c = r\,c(t) - \frac{\Lambda}{2V}\, M\big(\sigma + \kappa(T-t)\big)^2.$$

The analytical expressions presented above for the sensitivities of the option price will play a central role in the approximation of option prices in Section 8. In particular, we will show how these Greeks can be used to construct fast and accurate approximations of option prices. This forward-looking use of sensitivities will allow us to efficiently capture the effects of parameter changes on pricing. Table 2 presents the analytical expressions for each Greek under each model specification, illustrating their variations across different models.

5 Data

To calibrate and validate the model's ability to fit both futures prices and option implied volatilities across different maturities and moneyness levels, we gather daily data on the HH natural gas futures and associated options, covering $1,361$ trading days, equivalent to approximately 5.4 years, from January 2, 2020 to May 30, 2025. The HH natural gas futures and options contracts are listed on the NYMEX, part of the CME Group, and quoted in US dollars and cents per MMBtu. Data is sourced from Eikon Refinitiv.

This period encompasses several extraordinary events in natural gas markets, including extreme weather events such as Winter Storm Uri in 2021, the energy crisis triggered by the Russia–Ukraine war starting in 2022, and subsequent geopolitical tensions and supply disruptions up to 2025. These events generated unprecedented volatility episodes and make the sample particularly well-suited to evaluate models under both stable and stressed market conditions.

5.1 Futures

In the market, we observe HH physical futures contracts, denoted by the root "HH" followed by a single-letter month code [9] and the two-digit year of delivery. To construct a continuous series of constant-maturity futures, a daily roll is performed. On each trading day t, the front-month contract is the one maturing in the current month (or next month if t is on or after the expiration roll date). The roll date for month X is defined as the third-to-last business day of month X, which is the expiration date for the physical contract.

Throughout this thesis, we work with these constructed HH generic futures contracts, denoted by $\text{HHc1}, \text{HHc2}, \ldots, \text{HHc36}$ ranked by TTM.[10] Specifically, HHc1 is always the contract with the nearest expiration date (also known as the front-month), HHc2 is the second-nearest contract, and so on through HHc36. This procedure yields $1,252$ trading days multiplied by 36 contracts, giving $48,996$ futures price observations, all of which are non-missing (no blanks or zeros). For

[9] **F** = January, **G** = February, **H** = March, **J** = April, **K** = May, **M** = June, **N** = July, **Q** = August, **U** = September, **V** = October, **X** = November, and **Z** = December. The letter refers to the delivery month, however the contract actually expires on the third-to-last business day of the preceding month.

[10] For instance, on December 15, 2024 the front-month generic contract HHc1 corresponds to the physical contract HHF25; on the expiration day of December 2024, it rolls into HHG25, so from that date until the next expiration, HHc1 refers to the January 2025 contract.

the calibration and empirical analysis, we narrow our focus to the front-six HH generic futures contracts (HHc1–HHc6) and the ninth-month contract (HHc9) to better capture and illustrate stylized features of commodity markets. Figure 3 illustrates the evolution of natural gas futures prices for contracts HHc2, HHc4, and HHc6 over our sample period. As summarized in Table 3, we report the key descriptive statistics for the cleaned HH Generic futures prices across the six front-month contracts (HHc1–HHc6) and the ninth-month contract (HHc9). For each contract, the table lists the total number of observations, the mean, median, standard deviation, minimum, and maximum prices.

5.2 Options

The initial options dataset comprises call and put options on the first 24 futures contracts (HHc1–HHc24) at eleven different strikes determined by an offset-tick corresponding to increments of 5 cents in US dollars. For consistency with market liquidity and to focus on the most relevant moneyness levels, our analysis later concentrates on the six strikes nearest to the at-the-money (ATM) level. For contracts HHc25–HHc36, no option data is available. This results in $1,361$ trading days by 264 option contracts, for a total of $359,304$ option quotes. Of these, $136,600$ prices are blank or missing, and an additional $154,502$ are identically zero, leaving only $68,202$ observations available across $1,252$ trading days.

We restrict our analysis to call options and omit put options for two reasons. First, the available put quotes contained numerous recording errors, such as a large number of missing quotes, together with implausible prices[11], which compromise data reliability. Second, put prices do not provide additional market information, since they can be easily obtained from call prices with the same strike and maturity via put–call parity. Furthermore, we exclude in-the-money (ITM) calls because their premiums include an intrinsic value component that does not depend on the volatility of the underlying[12], this filtering step is standard in the option pricing literature. By contrast, the time value of an out-of-the-money (OTM) option grows with the market's expectation of future volatility, making it the relevant factor for model calibration.

Finally, after completing the data filtering stage, we conduct a quality-inspection process to identify and remove outliers that could compromise our analysis. We identify 454 erroneous option prices, leaving a final dataset of $19,796$ observations.

Figure 6 illustrates the historical evolution of option prices on HHc2, HHc4, and HHc6 contract at offset-tick 0, over our sample period. Complementarily, Table 4 outlines the descriptive statistics for the corresponding call option prices, displaying overall counts and summary measures (mean, median, standard deviation, minimum, and maximum) for all option observations, along with the breakdown of ATM and OTM counts. In addition, Table 5 reports, for each HH contract and each offset-tick combination, the number of available filtered option contracts,

[11] We detect inconsistencies by comparing implied volatilities, for options with the same strike and maturity, call and put implied volatilities must coincide.

[12] The intrinsic value of a call option is $\max\{F(t,T)-K,0\}$, representing the immediate exercise payoff.

this breakdown provides a clearer view of the cross-sectional coverage of the dataset across maturities and strikes.

6 Calibration and Validation

To assess the performance of our one-factor models (Bla76, CS99b, and CS+H), we divide the dataset into two non-overlapping samples: i) one period used to calibrate model parameters in-sample, and ii) a second period used to validate out-of-sample pricing accuracy. This split allows us to expose the models to historical stress events during calibration, and subsequently observe their behavior under new conditions in the test set. Our sample period is on a daily basis.

6.1 Sample Periods

6.1.1 In-Sample

The in-sample period considered spans from January 1, 2020, to December 31, 2024; and is at daily frequency, this results in $1,157$ trading days. The final dataset throughout this period comprises $17,685$ option observations, corresponding to 89.3% of the total . Within this interval, models are calibrated to daily futures prices and corresponding call-option implied volatilities. By calibrating over a relatively long sample (four full calendar years), the models are exposed to multiple unforeseen shocks that characterized the natural gas market.

6.1.2 Out-of-Sample

For the out-of-sample analysis, the period considered spans from January 2, 2025, to May 30, 2025, and is at daily frequency, this results in 95 trading days. The final dataset throughout this period comprises $2,111$ option observations, corresponding to 10.7% of the total. We hold all parameters fixed to their calibrated values and evaluate the models' pricing errors within this interval.

6.2 Calibration Methodology

To calibrate the parameters to our models in the in-sample period, we solve a non-linear least-squares problem using the `least_squares` function from the `scipy.optimize` package in Python. We denote $C_i^{\text{mdl}}(\omega)$ and C_i^{mkt} the model-implied and market-observed prices for call options, respectively, $i = 1, \ldots, N$. The calibrated parameter vector $\hat{\omega} = \{\sigma, \alpha, \kappa\}$ is obtained by minimizing the difference

$$\hat{\omega} \equiv \arg\min_{\omega} \sum_{i=1}^{N} \left(C_i^{\text{mdl}}(\omega) - C_i^{\text{mkt}}\right)^2,$$

N denotes the number of observations included in the calibration, which depends on the specific method applied. For each of the models and within the in-sample period, we implement four calibration methods:

1. **Method 0.** It consists of calibrating the entire universe of options simultaneously, finding one global parameter set $\hat{\omega}$.

2. **Method 1.** It consists of calibrating separately for each trading date t (that is, grouping observations by date and fitting one parameter set $\hat{\omega}_t$ per day).

3. **Method 2.** It consists of calibrating by both date t and moneyness category (ATM vs OTM) (that is, fitting one parameter set $\hat{\omega}_{t,m}$ per date t and moneyness bucket n). Strikes K are defined relative to the underlying futures price $F(t,T)$ as follows:

$$K \;=\; \text{round}\big(F(t,T)\big)_{\text{2d.p.}} \;+\; \text{offset tick} \times 0.05,$$

   where "round$_{\text{2d.p.}}$" denotes rounding $F(t,T)$ to its second decimal place, and offset_tick $\in \{0,1,2,3,4,5\}$. In particular, we consider the option to be ATM when offset_tick $\in \{0,1,2\}$, and OTM when offset_tick $\in \{3,4,5\}$.

4. **Method 3.** It consists of calibrating by both date t and offset-tick category (that is, fitting one parameter set $\hat{\omega}_{t,m}$ per date t and offset-tick bucket m).

We implement these four calibration methods to evaluate the flexibility and robustness of the models under different estimation strategies: Method 0 provides a global calibration to assess overall model consistency across the complete dataset; Method 1 allows us to capture daily variations in market conditions and volatility structures; Method 2 enables a deeper analysis of the models' ability to capture differences across distinct moneyness categories, offering insights into their performance in fitting both ATM and OTM options separately; finally, Method 3 further subdivides moneyness into six offset-tick buckets, thereby endowing it with greater flexibility than Method 2.

We do not consider alternative grouping schemes such as by individual contract (i.e. by expiration date) because in both CS99b and CS+H frameworks, parameters α and κ are specified as functions of each contract's TTM. Grouping observations by contract/expiration date would fix the TTM across all options in each group, thereby preventing these parameters from adapting to variations in TTM – the very feature we aim to capture in our models. Consequently, calibrating α and κ on a fixed-expiry basis would undermine the TTM structure, central to our analysis.

6.3 Validation Methodology

To validate model robustness, we hold all parameters fixed at their calibrated values and evaluate model pricing errors on option data within the out-of-sample interval. We group by contract

characteristics and compute the corresponding error metrics for each group. The grouping variables are defined as follows:

1. **Group A:** By contract identifier. We aggregate all observations per generic contract (e.g. HHc1, HHc2,...).
2. **Group B:** By moneyness category. We partition the sample into ATM and OTM options.
3. **Group C:** By offset-tick. We isolate observations by offset-tick (e.g. tick 0, 1,...).
4. **Group D:** By contract and offset-tick. We form joint buckets defined by both contract identifier and offset-tick.

6.4 Pricing Errors

To assess model performance, we employ two standard error metrics. The Root Mean Squared Error (hereafter RMSE) measures the square root of the average squared deviations between model-predicted prices C_i^{mdl} and market-observed prices C_i^{mkt}, the Mean Absolute Error (hereafter MAE) measures the average absolute deviation between predictions and observations.[13] Both metrics provide complementary insights: RMSE penalizes large errors more heavily due to the squaring, whereas MAE gives equal weight to all deviations.

7 Calibration and Validation Results

The purpose of this section is twofold. First and in-sample, we study the models' performance by means of a calibration procedure. Second and out-of-sample, we carry out a validation exercise in which we use the parameters obtained in the first stage.

7.1 In-Sample Performance

We begin by examining the in-sample calibration results, which provide a direct assessment of how well each model can reproduce observed option prices under the different calibration schemes or methods. This analysis not only establishes the relative ranking of the models but also highlights the importance of the calibration granularity and the model's behavior during periods of market stress.

[13] These metrics are computed as $RMSE = \sqrt{\frac{1}{N}\sum_{i=1}^{N}\left(C_i^{\text{mdl}} - C_i^{\text{mkt}}\right)^2}$, $\quad MAE = \frac{1}{N}\sum_{i=1}^{N}\left|C_i^{\text{mdl}} - C_i^{\text{mkt}}\right|$.

7.1.1 Relative Model Ranking

In-sample pricing error metrics (MAE and RMSE) by calibration method and model specification are reported in Table 6. They reveal a key insight, in particular a consistent ranking emerges across the more flexible calibration schemes (Methods 1, 2, and 3), where the hierarchy $Error_{CS+H} < Error_{CS99b} < Error_{Bla76}$ holds for both error metrics. To illustrate this visually, we plot the historical evolution of MAE and RMSE for each model under Methods 1, 2, and 3 in Figures 7 and 8, respectively. The CS+H model is plotted last to enhance visual comparison. We can observe that CS+H consistently shows the lowest error profile across most periods.

Building on this ranking, the largest improvement occurs under Method 3, where CS+H reduces both MAE and RMSE by more than one third relative to Bla76 and by around 13% relative to CS99b. The results are consistent across all calibration methods, underscoring the material benefits of combining richer volatility dynamics with high-resolution calibration.

7.1.2 Global vs Flexible Calibrations

Under the global calibration Method 0, CS+H and CS99b models exhibit virtually identical in-sample error metrics, as reported in Table 6. This implies that, in this case, the CS+H specification provides no incremental value, and the model effectively reduces to CS99b. This equivalence is further confirmed by the volatility term-structures plotted for all models using Method 0 parameters in Figure 9a, which reveals an almost complete overlap between the CS99b and CS+H curves. This outcome is expected as Method 0 relies on a single parameter to explain the whole in-sample period, which limits the model's ability to exploit the additional flexibility of CS99b and specially that of CS+H.

Under Methods 1, 2, and 3, the variance surface produced by the CS+H specification consistently displays the characteristic hump shape. This outcome is consistent with our expectations, as the calibration framework allows for greater flexibility – the hump parameter can be fully exploited to capture non-monotonic term-structures. Figures 9, 10, and 11 illustrate this feature for August 14, 2020.[14]

Increasing calibration granularity remarkably improves model performance – a detailed quantification of this impact is displayed in Table 7: i) transitioning from a global calibration approach (Method 0) to a daily calibration scheme (Method 1) produces the largest improvement, with errors dropping by roughly two-thirds across all models; ii) the introduction of an additional segmentation by moneyness (Method 2) provides further but more modest reductions; iii) further subdividing by offset-tick (Method 3), delivers the best overall fit.

Although the transition from Method 0 to Method 1 produces the biggest reduction, it starts from relatively large error levels. By contrast, the refinement from Method 2 to Method 3 applies to already low errors, pushing them to their lowest observed values – this makes this refinement particularly impactful. For context, the transition from Method 0 to Method 3 reduces MAE by

[14]We choose this date because it is one of our extreme-volatility dates, further discussed in Section 7.1.3.

78.5%, 83.9%, and 86.1% for Bla76, CS99b, and CS+H models, respectively; and RMSE by 85.0%, 88.1%, and 89.7%, respectively. These results highlight that calibration flexibility plays a decisive role in exploiting the expressive power of the models, particularly for CS+H.

These findings suggest that the benefits of the additional structural complexity in CS+H only becomes apparent when the calibration framework is sufficiently flexible to capture local features in the data, that is, for Method 3. Without such granularity, the extra degrees of freedom embedded in the model do not deliver its full potential.

Overall, the results indicates that CS+H is the most appropriate model when calibration is performed under Method 3, as this setting allows the hump component to be fully exploited. Under Methods 0–2, CS+H continues to rank as the best performing model, but the benefits relative to CS99b are less evident and, in the case of Method 0, virtually disappear.

7.1.3 High-Volatility Episodes

The amplitude of the hump becomes more pronounced during episodes of severe market stress, such as climatic disruptions, geopolitical tensions, or idiosyncratic shocks. Precisely in these stressed periods, the CS+H model demonstrates its added value by delivering lower in-sample errors. In this case, we select the high-volatility windows related to the following episodes:

(a) **Gulf Coast production disruptions**: August, 2020. Production disruptions at US Gulf Coast facilities constrained HH supply and drove prices upward.

(b) **Winter storm Uri**: February 4–17, 2021. Unprecedented cold temperatures in Texas (US) and surrounding regions led to power outages, supply disruptions, and sharp price spikes.

(c) **European supply anxiety**: April 7–8, 2022. Escalating geopolitical tensions and supply anxieties in Europe intensified market uncertainty and triggered price spikes.

(d) **Middle-East conflict shock**: January 2–4, 2024. Hamas attacks in the Middle-East elevated geopolitical risk premia across energy markets.

(e) **Non-renewal of Ukraine transit deal**: August 27, 2024. President Zelensky announced that Ukraine would not extend the gas transit agreement with Russia beyond its expiration on December 31, 2024. This position was later reiterated by Prime Minister Shmyhal on December 16, 2024, and confirmed by President Putin during December 18–23, 2024, stating there would be no new agreement after the contract's expiration.

Tables 8, 9, and 10 quantify the reductions in error metrics achieved by CS+H relative to the benchmark models during high-volatility windows, under each calibration Method. The results reveal substantial performance improvements, in each window, the CS+H model achieves in-sample error reductions, highlighting its superior capacity to adapt to sudden surges in market uncertainty.

7.2 Out-of-Sample Performance

For the out-of-sample evaluation, we reserve a test set of 2,111 option quotes beyond the in-sample period, and assess the pricing performance of the global calibration scheme (Method 0). We use the calibrated parameter vector $\hat{\omega}$, obtained in the in-sample analysis under Method 0 for each specification (see Table 11), in order to price the options in this hold-out period. We then calculate the pricing errors following the validation methodology introduced in Section 6.3.

Table 12 reports errors by Group A. The results reveal a clear TTM effect: for nearest-term contracts (HHc1–HHc4), Bla76 yields the lowest errors; for larger maturity contracts, the CS99b and CS+H specifications overtake Bla76, reducing MAE by up to 65.8% and 61.11%, respectively. However, CS+H offers neglibible improvements over CS99b, which means that this turning point is driven primarily by the Samuelson parameter α (that is, the additional parameter κ contributes no measurable benefit in this grouping).

Table 13 displays the results by Group B. RMSE is virtually identical across all three models, but Bla76 delivers a 20% reduction in MAE, indicating that it better mitigates large mispricing events emphasized by a non quadratic loss.

As reported in Table 14, by Group C Bla76 achieves the lowest MAE and RMSE across most offset-tick buckets. By contrast, CS+H essentially matches CS99b but offers no improvement.

Finally, Table 15 reports MAE and RMSE by Group D. A pronounced stair-step pattern emerges, CS99b and CS+H models are heavily penalized at the shortest TTM but gain steadily with tenor, overtaking Bla76 from HHc5 onward. This provides evidence that a single global parameterization cannot uniformly span the entire term-structure without sacrificing accuracy at the long end.

In conclusion, the out-of-sample analysis under the global calibration (Method 0) highlights the limitations of relying on a single parameter set to capture the full complexity of the natural gas volatility surface. Out-of-sample validation is only feasible with Method 0, since local methods (e.g., daily or bucket-specific calibrations) produce multiple parameter sets that cannot be meaningfully extended to the entire hold-out sample. Bla76 dominates at short maturities and across most offset-ticks. However, CS99b and CS+H outperform Bla76 at longer maturities, reflecting the importance of the Samuelson effect in modeling the term-structure of volatility. At this level of calibration, the hump parameter cannot be effectively exploited, which explains why CS+H provides no advantage over CS99b. This does not imply that the hump parameter lacks explanatory power, but rather that its benefits can only be identified under more flexible calibration schemes.

8 Approximating Option Prices on Futures Using Greeks

In this section we evaluate the extent to which the standard Greeks can approximate short-term changes in option prices, using observable ex-post variations in the underlying risk factors.

Specifically, we assess whether changes in futures prices and implied volatilities between two consecutive days can explain the observed variation in option values within the same period. This analysis provides insight into the explanatory power of first- and second-order sensitivities under relatively stable market conditions, while also allowing us to detect potential deviations associated with more abrupt events, such as jumps or spikes. For this part of the analysis, we use the results obtained from the in-sample calibration under Method 3, since this is the most flexible approach.

Let dF denote the daily change in the futures price of the underlying asset, and let $d\sigma$, $d\alpha$, and $d\kappa$ represent the daily change in the parameters σ, α, and κ of the option. We denote the values of the Delta, Gamma, and Vega of the call option computed on the previous day by Δ_c, Γ_c, and ν_c, correspondingly. The Taylor-based Delta-Gamma-Vega approximation yields:

$$
\begin{aligned}
c_{\text{approx}}(t,T,K) &= c(t-1,T,K) + dF\,\Delta_c + \tfrac{1}{2}dF^2\,\Gamma_c + d\sigma\,\nu_c^{\sigma} + d\alpha\,\nu_c^{\alpha} + d\kappa\,\nu_c^{\kappa},\\
dF &= F(t,T) - F(t-1,T),\\
d\sigma &= \sigma(t,T,K) - \sigma(t-1,T,K),\\
d\alpha &= \alpha(t,T,K) - \alpha(t-1,T,K),\\
d\kappa &= \kappa(t,T,K) - \kappa(t-1,T,K).
\end{aligned}
$$

We iterate this approximation over a rolling window of trading days from January 1, 2020 to December 31, 2024, (the in-sample period) focusing only on ATM call options (in order to minimize the effects of strike-dependent skew or smile distortions) on HHc3. Our objective is to compare the approximated option price $c_{\text{approx}}(t)$ to its quoted market value $c(t)$ on day t, and to quantify the approximation error[15], persistent alignment between the approximated and observed prices indicates that the evolution of option value is well captured by the Greeks; oppositely, significant discrepancies may signal the presence of discontinuities or market events, such as price jumps or volatility shocks, that are not captured by the smooth local dynamics implied by the Greeks. This error data can then be analyzed to assess the model's stability across contracts with different maturities and strikes.

To ensure statistical robustness and mitigate sample noise, we focus the analysis on the "HHc3 + Offset-Tick" combinations,[16] which according to Table 5 provide the richest data availability. In particular, the configurations HHc3 + 0, HHc3 + 1, and HHc3 + 2 comprise 811, 865, and 879 observations, respectively. This subset therefore serves as our primary empirical basis, offering both sufficient sample size and coverage across short maturities while maintaining homogeneity in contract characteristics. By concentrating on these richly populated data, we can draw more reliable conclusions regarding the comparative precision of our approximation across two distinct maturities.

[15] Calculated as $\text{Error}(t) = c_{\text{approx}}(t) - c(t)$.

[16] Although the discussion in this section concentrates on this combination, the analysis was conducted for all available Contract + Offset combinations in our dataset.

The results reported in Table 16 indicate the superior precision of the CS+H model relative to both the Bla76 and CS99b benchmarks. Across every contract + offset-tick configuration examined, CS+H achieves the lowest MAE and RMSE. Notably, the only exception arises for HHc3 + 0, where CS+H's RMSE is marginally higher than CS99b's. This slight RMSE degradation appears driven by idiosyncratic sample variation and does not undermine the overall dominance of CS+H in approximation accuracy.

For the selected combinations, we plot each model's absolute approximation error. Figure 12 reports the 120-day rolling median of these errors: panel (a) corresponds to HHc3+0, panel (b) to HHc3+1, and panel (c) to HHc3+2. In all cases, the CS+H model achieves the lowest, or jointly lowest absolute error, as reflected in the rolling-median profiles and consistent with the quantitative results. In this way, we complement the quantitative error metrics with a direct visual comparison, confirming not only that CS+H tracks the data most closely, but also illustrating where and by how much the other two benchmarks deviate over time.

In light of these quantitative and visual diagnostics, we conclude that the CS+H model clearly outperforms the two benchmarks. Its lower MAE and RMSE across the selected Contract + Offset-Tick combinations, together with its markedly tighter fit to the option-price paths, demonstrate that incorporating the additional sensitivity terms inherent to CS+H yields a far more faithful replication of market dynamics than either the classical Bla76 or the CS99b model. Consequently, CS+H should be regarded as the preferred approximation framework for short-term option price forecasting under the moderate market conditions studied here.

9 Conclusions and Further Research

In this work we propose a new futures-based model for option pricing on natural gas futures. The model was specifically designed to capture the empirically observed hump-shaped feature in implied volatilities. Its empirical performance has been analyzed in comparison with benchmark models widely used in the literature. The CS+H specification naturally nests the Bla76 and CS99b models, which therefore serve as natural reference points for the empirical analysis.

Beyond improvements in pricing accuracy, another central contribution of this thesis is to document and model the empirical coexistence of two distinct volatility dynamics in natural gas markets: the Samuelson effect and the hump-shaped pattern in option implied volatilities. While the Samuelson effect dominates in many trading days, our panel evidence shows that non-monotonic, hump-shaped term structures appear nearly as often. Moreover, when option implied volatilities are obtained from calibrations grouped by contract, the resulting variance surface systematically accentuates the hump-shaped feature. This evidence validates the empirical motivation behind the CS+H specification, by extending the volatility term-structure beyond pure exponential decay, the model is able to accommodate both dynamics within a unified framework. This flexibility is particularly relevant in stressed market conditions, where humps tend to be more pronounced and standard models fail to capture the observed dynamics.

The results show that the CS+H specification delivers consistently more accurate pricing of options on NYMEX HH natural gas futures, with lower error values and better model performance in terms of MAE and RMSE than the two benchmarks Bla76 and CS99b. By enriching the deterministic volatility term-structure to capture the empirically observed humps in mid-tenor implied variances, CS+H better aligns model-implied and market-observed option prices across a wide range of maturities and strikes.

Another important result concerns the crucial role of calibration flexibility. In this work we propose a multiple-dimension calibration analysis, which is quite flexible and goes from a minimum to a maximum granularity level. Under a global calibration (Method 0), CS+H offers no material advantage over the CS99b specification and yields only marginal improvements. As we introduce additional degrees of freedom all the way to further differentiating across offset-tick and date buckets (Method 3), pricing errors decline monotonically. This shows that a greater calibration granularity is essential to exploit the full expressive power of the hump parameter, where CS+H reduces both MAE and RMSE by more than one third relative to Bla76 and by around 13% relative to CS99b.

These performance gains are robust across the in-sample test, as well as in our analysis of approximation using each model Greeks. This stability under varying market regimes, including stress episodes driven by weather shocks and supply disruptions, demonstrates that CS+H not only provides more accurate fits but also produces more reliable risk sensitivities. Overall, the CS+H model strikes a parsimonious balance between analytical tractability and empirical flexibility, offering both academics and practitioners a superior tool for valuation, calibration, and risk management in natural gas derivatives markets.

As future lines of research, the CS+H framework could be extended to a multi-factor model, capable of capturing regime-specific variations in the forward-curve beyond a single hump. Another avenue is to incorporate jump dynamics to better accommodate abrupt market moves. A further extension would be to incorporate seasonality effects, which are highly relevant in natural gas markets due to predictable demand fluctuations across winter and summer months. Finally, assessing the model's economic performance by analyzing P&L series and conducting a Value-at-Risk (VaR) analysis.

References

Black, F. (1976), 'The pricing of commodity contracts', Journal of Financial Economics **3**(1), 167–179.

Casassus, J. & Collin-Dufresne, P. (2005), 'Stochastic convenience yield implied from commodity futures and interest rates', The Journal of Finance **60**(5), 2283–2331.

Cheng, B., Nikitopoulos, C. S. & Schlögl, E. (2018), 'Pricing of long-dated commodity deriva-

tives: Do stochastic interest rates matter?', Journal of Banking & Finance **95**, 148–166. Commodity and Energy Markets.

Chiarella, C., Kang, B. & Nikitopoulos, C. (2013), 'Humps in the volatility structure of the crude oil futures market: New evidence', Energy Economics **40**, 989–1000.

Clewlow, L. & Strickland, C. (1999a), A multi-factor model for energy derivatives, Research Paper Series 28, Quantitative Finance Research Centre, University of Technology, Sydney.

Clewlow, L. & Strickland, C. (1999b), Valuing energy options in a one factor model fitted to forward prices, Research Paper Series 10, Quantitative Finance Research Centre, University of Technology, Sydney.

CME Group (2025), 'Introduction to natural gas', `www.cmegroup.com/education/courses/introduction-to-natural-gas.html`. CME Institute educational course overview.

Crosby, J. (2008), 'A multi-factor jump-diffusion model for commodities', Quantitative Finance **8**(2), 181–200.

Crosby, J. & Frau, C. (2022), 'Jumps in commodity prices: New approaches for pricing plain vanilla options', Energy Economics **114**, 106302.

Energy Institute (2025), Statistical review of world energy, Technical Report 74th Edition, Energy Institute.
URL: *www.energyinst.org/statistical-review*

Frau, C. & Fanelli, V. (2023), 'Seasonality in commodity prices: new approaches for pricing plain vanilla options', Annals of Operations Research **336**, 1089–1131.

Geman, H. (2000), Scarcity and price volatility in oil markets, Trading technical report, Electricité de France, Paris.

Gibson, R. & Schwartz, E. S. (1990), 'Stochastic convenience yield and the pricing of oil contingent claims', The Journal of Finance **45**(3), 959–976.

Kang, B., Nikitopoulos, C. S. & Prokopczuk, M. (2020), 'Economic determinants of oil futures volatility: A term structure perspective', Energy Economics **88**, 104743.

Lucía, J. J. & Schwartz, E. (2002), 'Electricity prices and power derivatives: Evidence from the nordic power exchange', Review of Derivatives Research **5**(1), 5–50.

Mercurio, F. & Moraleda, J. (2000), 'An analytically tractable interest rate model with humped volatility', European Journal of Operational Research **120**(1), 205–214.
URL: *https://www.sciencedirect.com/science/article/pii/S0377221798003828*

Moraleda, J. M. & Vorst, T. C. (1997), 'Pricing american interest rate claims with humped volatility models', Journal of Banking & Finance **21**(8), 1131–1157.

Schneider, L. & Tavin, B. (2018), 'From the samuelson volatility effect to a samuelson correlation effect: an analysis of crude oil calendar spread options', Journal of Banking & Finance **95**, 185–202.

Schneider, L. & Tavin, B. (2021), 'Seasonal volatility in agricultural markets: Modelling and empirical investigations', Annals of Operations Research **334**(1), 7–58.

Schwartz, E. S. (1997), 'The stochastic behavior of commodity prices: Implications for valuation and hedging', The Journal of Finance **52**(3), 923–973.

Schwartz, E. S. & Smith, J. E. (2000), 'Short-term variations and long-term dynamics in commodity prices', The Journal of Finance **46**(7), 893–911.

Trolle, A. B. & Schwartz, E. S. (2009), 'Unspanned stochastic volatility and the pricing of commodity derivatives', Review of Financial Studies **22**(11), 4423–4461.

A Tables and Figures

Table 1: Stochastic differential equations and variance expressions for each model.

Model	**SDE for** $F(t,T)$	**Integrated Variance**
Bla76	$\frac{dF(t,T)}{F(t,T)} = \sigma\, dW_t$	$V^2 = \sigma^2(T-t)$
CS99b	$\frac{dF(t,T)}{F(t,T)} = \sigma\, e^{-\alpha(T-t)}\, dW_t$	$V^2 = \frac{\sigma^2}{2\alpha}\big(1-M\big)$
CS+H	$\frac{dF(t,T)}{F(t,T)} = \big(\sigma + \kappa(T-t)\big)\, e^{-\alpha(T-t)}\, dW_t$	$V^2 = A\big(1-M\big) - BM$
		$A = \frac{1}{2\alpha}\left(\sigma^2 + \frac{\sigma\kappa}{\alpha} + \frac{\kappa^2}{2\alpha^2}\right)$
		$B = \frac{\kappa(T-t)}{\alpha}\left(\sigma + \frac{\kappa(T-t)}{2} + \frac{\kappa}{2\alpha}\right)$

NOTES: In this table we showcase the dynamics and integrated variance of every model used in this work. Here V^2 is the total variance over the interval $[t,T]$. This variance enters directly into the option pricing formulas, for instance in equation (3.6), and is also used in the derivation of the Greeks and related sensitivity measures.

Table 2: Greek analytical expressions by model.

Greek	**Bla76**	**CS99b**	**CS+H**
Δ_c	$e^{-r(T-t)}\mathcal{N}(d_1)$	$e^{-r(T-t)}\mathcal{N}(d_1)$	$e^{-r(T-t)}\mathcal{N}(d_1)$
Γ_c	$\frac{e^{-r(T-t)}\mathcal{N}'(d_1)}{F(t,T)V}$	$\frac{e^{-r(T-t)}\mathcal{N}'(d_1)}{F(t,T)V}$	$\frac{e^{-r(T-t)}\mathcal{N}'(d_1)}{F(t,T)V}$
ρ_c	$-c(t)(T-t)$	$-c(t)(T-t)$	$-c(t)(T-t)$
ν_c	ν_c^σ	$\nu_c^\sigma+\nu_c^\alpha$	$\nu_c^\sigma+\nu_c^\alpha+\nu_c^\kappa$
ν_c^σ	$\frac{\Lambda V}{\sigma}$	$\frac{\Lambda V}{\sigma}$	$\frac{\Lambda}{2V\alpha}\Big(\big(\sigma+\frac{\kappa}{2\alpha}\big)(1-M)-\kappa(T-t)M\Big)$
ν_c^α	—	$\Lambda V\left(\frac{M(T-t)}{1-M}-\frac{1}{2\alpha}\right)$	$\frac{\Lambda}{2V\alpha^2}\left(\big(-\frac{\sigma^2}{2}-\frac{\sigma\kappa}{\alpha}-\frac{3\kappa^2}{4\alpha^2}\big)(1-M)+M(T-t)\Big(\kappa(\sigma+\frac{\kappa(T-t)}{2}+\frac{\kappa}{\alpha})+2\alpha^2(B+A)\Big)\right)$
ν_c^κ	—	—	$\frac{\Lambda}{2V\alpha}\Big(\big(\frac{\sigma}{2\alpha}+\frac{\kappa}{2\alpha^2}\big)(1-M)-(T-t)\big(\sigma+\kappa(T-t)+\frac{\kappa}{\alpha}\big)M\Big)$
θ_c	$rc(t)-\Lambda\frac{V}{2(T-t)}$	$rc(t)-\alpha\Lambda V\frac{M}{1-M}$	$rc(t)-\frac{\Lambda}{2V}M\big(\sigma+\kappa(T-t)\big)^2$

NOTES: In this table we showcase the analytical expressions of every Greek by model. Formulas are presented with A,B,M defined in equation (3.2), $c(t)$ as in equation (3.6), and Λ as in equation (4.1). The specific values V for each model are provided in Table 1, while the derivations of all Greeks can be found in Section 4.

Table 3: Descriptive statistics of HH generic futures prices by contract.

Contract	Count	Mean	Median	Std. Dev.	Min	Max
HHc1	196	2.8427	2.6730	0.7505	1.6530	4.4910
HHc2	1,125	3.1314	2.8950	1.2093	1.5440	9.3440
HHc3	1,197	3.2190	2.8430	1.3757	1.6050	9.7100
HHc4	1,108	3.1802	2.9250	1.2273	1.7250	9.5640
HHc5	1,054	3.1683	2.9280	1.1275	1.9070	9.5320
HHc6	994	3.2208	2.9190	1.1002	1.9260	9.3180
HHc9	602	3.2113	2.9280	0.9063	2.1610	8.0670
Total	6,276	3.1760	2.9190	1.2108	1.5440	9.7100

NOTES: In this table we showcase the descriptive statistics for our HH generic futures prices by contract.

Table 4: Descriptive statistics of call option prices by contract.

Contract	Count	ATM	OTM	Mean	Median	Std. Dev.	Min	Max
HHc1	828	357	471	0.0808	0.0690	0.0596	0.0010	0.3000
HHc2	2,293	1,616	677	0.2376	0.1950	0.1924	0.0350	1.4110
HHc3	5,533	2,763	2,770	0.3134	0.2320	0.2945	0.0230	1.7550
HHc4	4,098	2,019	2,079	0.3375	0.2690	0.3023	0.0340	2.0730
HHc5	3,324	1,698	1,626	0.3600	0.2890	0.3041	0.0360	2.4890
HHc6	2,678	1,352	1,326	0.3897	0.3120	0.3154	0.0490	2.6250
HHc9	1,042	453	589	0.3871	0.3650	0.2369	0.0750	2.1330
Total	19,796	10,258	9,538	0.3220	0.2490	0.2897	0.0010	2.6250

NOTES: This table reports summary statistics for all call options on HH generic futures.

Table 5: Number of observations of call option prices per contract and offset-tick.

Offset-Tick	**HHc1**	**HHc2**	**HHc3**	**HHc4**	**HHc5**	**HHc6**	**HHc9**
0	0	1,023	811	631	541	435	25
1	115	178	865	612	501	441	195
2	119	171	879	609	506	353	173
3	110	167	869	613	496	411	170
4	101	155	869	660	508	424	163
5	91	142	846	649	480	381	197
Total	536	1,836	5,139	3,774	3,032	2,445	923

NOTES: This table reports, for each HH contract and each offset-tick, the count of available observations from January 1, 2020 to December 31, 2024.

Table 6: In-sample calibration errors.

Method	**MAE**			**RMSE**			**Δ MAE (%)**		**Δ RMSE (%)**	
	Bla76	CS99b	CS+H	Bla76	CS99b	CS+H	vs Bla76	vs CS99b	vs Bla76	vs CS99b
Method 0	0.1116	0.1108	0.1108	0.1723	0.1625	0.1625	−0.7264	−0.0036	−5.6653	−0.0018
Method 1	0.0467	0.0342	0.0310	0.0561	0.0407	0.0371	−33.5396	−9.0954	−33.7508	−8.8195
Method 2	0.0403	0.0293	0.0257	0.0461	0.0338	0.0295	−36.3438	−12.4010	−36.0453	−12.6199
Method 3	0.0240	0.0178	0.0154	0.0259	0.0193	0.0167	−35.9760	−13.5087	−35.4585	−13.4861

NOTES: This table reports the in-sample calibration metrics for three pricing models (Bla76, CS99b, and CS+H) across different calibration methods, alongside percentage changes of CS+H relative to Bla76 and CS99b.

Table 7: Impact of calibration methods on pricing accuracy.

Transition	**Δ MAE (%)**			**Δ RMSE (%)**		
	Bla76	CS99b	CS+H	Bla76	CS99b	CS+H
Method 0→1	-58.1626	-69.1899	-71.9912	-67.4625	-74.9399	-77.1496
Method 1→2	-13.6655	-14.1878	-17.3082	-17.6844	-17.0792	-20.5353
Method 2→3	-40.3834	-39.2711	-40.0390	-43.8429	-42.7603	-43.3277
Method 0→3	-78.4664	-83.9440	-86.1124	-84.9592	-88.1055	-89.7094

NOTES: This table reports the reductions (in %) in MAE and RMSE achieved by transitioning calibration schemes.

Table 8: Percentage improvements of CS+H vs benchmarks by Method 1.

Ref	**Date**	**Δ MAE (%)**		**Δ RMSE (%)**	
		vs Bla76	vs CS99b	vs Bla76	vs CS99b
(a)	03/08/2020	6.0473	-13.1412	-14.2610	-6.4563
	06/08/2020	-2.2937	-10.3775	-17.8984	-7.2917
	17/08/2020	-0.8701	-13.1388	-20.1628	-9.3356
	26/08/2020	4.6991	-12.5781	-15.9457	-7.2355
	27/08/2020	-72.1230	-27.5565	-70.5261	-30.2153
(b)	04/02/2021	-63.1155	-19.9946	-59.2366	-25.1851
	05/02/2021	-69.8506	-37.3917	-65.5701	-38.7869
	08/02/2021	-70.8210	-35.9757	-64.6615	-34.1892
	12/02/2021	-63.9932	-33.5117	-55.9368	-32.7209
	17/02/2021	-59.1692	-29.1868	-50.5061	-28.7621
(c)	07/04/2022	-96.5839	-86.1840	-97.0151	-87.7046
	08/04/2022	-89.4668	-13.3054	-88.7475	-15.6506
	11/04/2022	-99.9553	-99.7874	-99.9559	-99.7883
(d)	02/01/2024	-84.1404	-70.8126	-74.8004	-56.3304
	03/01/2024	-75.6725	-53.0266	-71.4833	-47.1628
	04/01/2024	-74.8159	-50.1626	-74.1146	-54.2491
(e)	18/12/2024	-85.4976	-60.7095	-83.8483	-57.7768
	19/12/2024	-70.7708	-41.4487	-69.7543	-40.1843
	20/12/2024	-70.7554	-40.8226	-68.2885	-39.0862
	23/12/2024	-63.9268	-36.1653	-62.7244	-35.9780

NOTES: This table reports the percentage improvements in RMSE and MAE of the CS+H model relative to the Bla76 and CS99b benchmarks. All results are based on an in-sample calibration using Method 1. The reference labels (a)–(e) correspond to the high-volatility episodes listed in Section 7.1.3.

Table 9: Percentage improvements of CS+H vs benchmarks by Method 2.

Ref	Date	Moneyness	Δ MAE (%)		Δ RMSE (%)	
			vs Bla76	vs CS99b	vs Bla76	vs CS99b
(a)	03/08/2020	ATM	3.7459	-7.1611	-16.0480	-5.0697
		OTM	0.0420	-0.3482	0.0428	-0.2086
	06/08/2020	ATM	0.3019	-3.7037	-19.5287	-5.5497
		OTM	-0.0296	-0.5299	0.0062	-0.5250
	17/08/2020	ATM	-0.0320	-0.0329	-0.0364	-0.0401
		OTM	-38.7986	-5.5906	-43.9636	-12.6170
	26/08/2020	ATM	-0.0384	-0.0412	-0.0332	-0.0352
		OTM	-50.8921	3.7754	-47.4544	-16.0514
	27/08/2020	ATM	-76.7529	-34.9973	-71.0961	-31.9950
		OTM	-73.7942	-59.9372	-69.3685	-55.1167
(b)	04/02/2021	ATM	-59.9804	-25.0873	-58.8938	-31.5191
		OTM	-66.0204	-31.7028	-69.0051	-42.7644
	05/02/2021	ATM	-64.3577	-35.8366	-65.5402	-45.4413
		OTM	-74.2381	-51.2076	-76.2758	-57.7449
	08/02/2021	ATM	-69.3273	-39.0317	-65.5630	-41.3656
		OTM	-75.7072	-54.3892	-76.4463	-56.6884
	12/02/2021	ATM	-58.0141	-31.0391	-55.4039	-36.9639
		OTM	-77.7199	-62.8689	-78.1093	-64.0179
	17/02/2021	ATM	-53.3581	-24.1351	-50.7984	-32.8254
		OTM	-72.8181	-57.1587	-75.2499	-62.0811
	23/11/2021	OTM	0.0033	0.0078	0.0000	0.0000
(c)	07/04/2022	ATM	-96.5839	-86.1840	-97.0151	-87.7046
	08/04/2022	ATM	-89.4668	-13.3054	-88.7475	-15.6506
	11/04/2022	ATM	-99.9553	-99.7874	-99.9559	-99.7883
(d)	02/01/2024	ATM	-76.9243	-62.5977	-69.6789	-53.8529
		OTM	-96.9227	-94.9503	-96.5190	-94.2333
	03/01/2024	ATM	-66.9659	-41.7166	-65.4165	-39.4640
		OTM	-94.7388	-91.5465	-94.9767	-91.7903
	04/01/2024	ATM	-71.0229	-48.4218	-70.5228	-50.6781
(e)	18/12/2024	ATM	-91.2742	-72.4924	-90.0741	-72.5811
		OTM	-85.1911	-71.9312	-83.2709	-68.8135
	19/12/2024	ATM	-69.8166	-39.9460	-70.5770	-42.1206
		OTM	-71.8979	-55.5382	-67.4862	-51.2130
	20/12/2024	ATM	-68.6886	-40.6398	-67.5940	-38.6342
		OTM	-86.1430	-78.8862	-83.2955	-74.9383
	23/12/2024	ATM	-65.1725	-42.6586	-65.7155	-44.8666
		OTM	-62.0894	-41.3841	-60.4356	-39.9495

NOTES: This table reports the percentage improvements in RMSE and MAE of the CS+H model relative to the Bla76 and CS99b benchmarks. All results are based on an in-sample calibration using Method 2. The reference labels (a)–(e) correspond to the high-volatility episodes listed in Section 7.1.3. An absence of an entry for a given moneyness level indicates that no data were available for that category on that date. It is worth noting that in some cases the reported improvements may take very small values, this occurs on days when only a limited number of option contracts (one to three) are available for that specific moneyness bucket.

Table 10: Percentage improvements of CS+H vs benchmarks by Method 3.

Ref	Date	Offset-Tick	Δ MAE (%)		Δ RMSE (%)	
			vs Bla76	vs CS99b	vs Bla76	vs CS99b
(e)	18/12/2024	0	-34.3266	-19.2617	-34.3693	-19.2820
		1	-43.3714	-26.2551	-34.4032	-18.4943
		2	-85.1720	-65.7166	-82.3185	-60.4212
		3	-67.2729	-45.0501	-64.3562	-41.8349
		4	-64.1039	-40.6801	-62.1788	-39.4592
		5	-52.2880	-32.4244	-50.8845	-30.7769
(e)	19/12/2024	0	-15.0639	-7.7437	-15.1398	-7.7784
		1	-69.2542	-40.2196	-66.7923	-36.8803
		2	-51.6459	-30.6947	-51.3745	-29.3878
		3	-43.1374	-24.7743	-40.6042	-22.5463
		4	-43.8287	-25.2080	-40.7344	-23.0965
		5	-52.3230	-31.3617	-51.5891	-30.3937
(e)	20/12/2024	0	-60.0083	-29.9977	-59.9167	-28.2505
		1	-52.4707	-31.2977	-51.6066	-29.3697
		2	-42.8992	-22.1568	-42.6104	-24.4154
		3	-40.9610	-20.8959	-41.4717	-23.5321
		4	-53.8405	-32.2263	-52.0165	-31.2998
(e)	23/12/2024	0	-52.7166	-31.6510	-50.5110	-28.6403
		1	-53.9191	-32.9090	-51.8132	-29.8395
		2	-43.0262	-21.9744	-41.5225	-23.0162
		3	-42.6055	-22.4248	-40.7224	-22.5557
		4	-50.0965	-29.9834	-48.9369	-27.8912
		5	-42.0614	-24.1230	-38.4911	-21.2286

NOTES: This table reports the percentage improvements in RMSE and MAE of the CS+H model relative to the Bla76 and CS99b benchmarks. All results are based on an in-sample calibration using Method 3. The reference label (e) corresponds to the high-volatility episode "Non-renewal of Ukraine transit deal" described in Section 7.1.3. No more windows are reported for space reasons.

Table 11: Parameters used for the out-of-sample analysis.

Model	**Bla76**	**CS99b**	**CS+H**
Parameters	σ	σ, α	σ, α, κ
Method 0	[0.6160]	[0.8799, 2.4073]	[0.8793, 2.6533, 0.2272]

NOTES: Let $\omega = \{\sigma, \alpha, \kappa\}$ be the set of model parameters. These are the values obtained from the calibration under Method 0 and used in the out-of-sample analysis.

Table 12: Results in the out-of-sample analysis – Group A.

Contract	MAE			RMSE			Δ MAE (%)		Δ RMSE (%)	
	Bla76	CS99b	CS+H	Bla76	CS99b	CS+H	vs Bla76	vs CS99b	vs Bla76	vs CS99b
HHc1	0.0260	0.0635	0.0634	0.0445	0.0726	0.0725	144.1417	−0.1407	63.0214	−0.1167
HHc2	0.0333	0.0950	0.0949	0.0491	0.1045	0.1045	185.0145	−0.0710	112.7479	−0.0576
HHc3	0.0517	0.1074	0.1074	0.0679	0.1161	0.1161	107.9418	−0.0040	71.0214	−0.0022
HHc4	0.0780	0.1004	0.1005	0.0958	0.1145	0.1145	28.8272	0.0300	19.6031	0.0237
HHc5	0.0977	0.0838	0.0838	0.1160	0.1029	0.1029	−14.2153	0.0290	−11.2781	0.0213
HHc6	0.1088	0.0643	0.0643	0.1276	0.0844	0.0844	−40.9345	−0.0017	−33.8545	−0.0030
HHc9	0.2317	0.0793	0.0792	0.2446	0.0951	0.0951	−65.8017	−0.0780	−61.1125	−0.0323

NOTES: This table reports MAE and RMSE by contract under out-of-sample global calibration (Method 0), alongside percentage changes of CS+H relative to Bla76 and CS99b.

Table 13: Results in the out-of-sample analysis – Group B.

Moneyness	MAE			RMSE			Δ MAE (%)		Δ RMSE (%)	
	Bla76	CS99b	CS+H	Bla76	CS99b	CS+H	vs Bla76	vs CS99b	vs Bla76	vs CS99b
ATM	0.0768	0.0929	0.0929	0.1051	0.1066	0.1066	20.9279	−0.0253	1.4568	−0.0148
OTM	0.0649	0.0828	0.0828	0.0954	0.0967	0.0967	27.4908	−0.0281	1.3507	−0.0176

NOTES: This table reports MAE and RMSE for ATM and OTM buckets under out-of-sample global calibration (Method 0), alongside percentage changes of CS+H relative to Bla76 and CS99b.

Table 14: Results in the out-of-sample analysis – Group C.

Offset-Tick	MAE			RMSE			Δ MAE (%)		Δ RMSE (%)	
	Bla76	CS99b	CS+H	Bla76	CS99b	CS+H	vs Bla76	vs CS99b	vs Bla76	vs CS99b
0	0.0873	0.1009	0.1009	0.1131	0.1143	0.1143	15.5595	−0.0149	1.0046	−0.0081
1	0.0731	0.0902	0.0902	0.1001	0.1043	0.1042	23.3173	−0.0299	4.1785	−0.0175
2	0.0717	0.0890	0.0889	0.1029	0.1022	0.1022	24.0292	−0.0307	−0.7046	−0.0191
3	0.0676	0.0867	0.0867	0.0977	0.1003	0.1003	28.2087	−0.0269	2.6023	−0.0163
4	0.0660	0.0814	0.0813	0.0970	0.0956	0.0956	23.2423	−0.0276	−1.4113	−0.0176
5	0.0606	0.0799	0.0799	0.0908	0.0937	0.0937	31.8196	−0.0302	3.1721	−0.0194

NOTES: This table reports MAE and RMSE by offset-tick under out-of-sample global calibration (Method 0), alongside percentage changes of CS+H relative to Bla76 and CS99b.

Table 15: Results in the out-of-sample analysis – Group D.

Contract	MAE			RMSE			Δ MAE (%)		Δ RMSE (%)	
	Bla76	CS99b	CS+H	Bla76	CS99b	CS+H	vs Bla76	vs CS99b	vs Bla76	vs CS99b
HHc1+1	0.0254	0.0663	0.0662	0.0412	0.0742	0.0741	161.0455	−0.1445	79.8172	−0.1267
HHc1+2	0.0283	0.0663	0.0662	0.0494	0.0761	0.0760	133.9936	−0.1375	54.0384	−0.1104
HHc1+3	0.0276	0.0672	0.0671	0.0470	0.0769	0.0768	143.3586	−0.1332	63.2358	−0.1097
HHc1+4	0.0256	0.0601	0.0600	0.0442	0.0688	0.0687	134.7630	−0.1405	55.4600	−0.1164
HHc1+5	0.0228	0.0567	0.0566	0.0395	0.0652	0.0651	147.9585	−0.1498	64.8457	−0.1224
HHc2+0	0.0365	0.0965	0.0964	0.0509	0.1061	0.1060	164.5113	−0.0680	108.4900	−0.0557
HHc2+1	0.0365	0.0979	0.0979	0.0515	0.1073	0.1073	168.2003	−0.0668	108.2138	−0.0550
HHc2+2	0.0343	0.0967	0.0966	0.0500	0.1059	0.1058	181.6876	−0.0683	111.5140	−0.0566
HHc2+3	0.0322	0.0937	0.0936	0.0487	0.1032	0.1032	191.2177	−0.0717	111.9469	−0.0585
HHc2+4	0.0298	0.0932	0.0931	0.0463	0.1027	0.1027	212.3500	−0.0760	121.5376	−0.0607
HHc2+5	0.0293	0.0908	0.0907	0.0460	0.1007	0.1007	210.0166	−0.0776	119.0639	−0.0609
HHc3+0	0.0623	0.1195	0.1194	0.0760	0.1267	0.1267	91.7266	−0.0033	66.6749	−0.0019
HHc3+1	0.0623	0.1151	0.1151	0.0760	0.1236	0.1236	84.6480	−0.0025	62.5496	−0.0015
HHc3+2	0.0513	0.1073	0.1073	0.0670	0.1156	0.1156	109.1039	−0.0033	72.4650	−0.0017
HHc3+3	0.0457	0.1015	0.1015	0.0631	0.1104	0.1104	121.8606	−0.0050	74.9389	−0.0030
HHc3+4	0.0456	0.1020	0.1020	0.0629	0.1110	0.1110	123.5698	−0.0042	76.3623	−0.0021
HHc3+5	0.0412	0.0977	0.0977	0.0594	0.1068	0.1068	137.3397	−0.0066	79.8586	−0.0034
HHc4+0	0.0930	0.1164	0.1164	0.1081	0.1284	0.1284	25.1740	0.0263	18.7868	0.0217
HHc4+1	0.0851	0.1057	0.1058	0.1000	0.1191	0.1192	24.2146	0.0280	19.1577	0.0227
HHc4+2	0.0786	0.1006	0.1007	0.0967	0.1144	0.1144	28.1052	0.0288	18.3702	0.0235
HHc4+3	0.0778	0.1007	0.1007	0.0950	0.1141	0.1141	29.4073	0.0306	20.1630	0.0243
HHc4+4	0.0654	0.0873	0.0874	0.0860	0.1028	0.1028	33.5208	0.0345	19.4916	0.0260
HHc4+5	0.0661	0.0904	0.0904	0.0852	0.1049	0.1049	36.7095	0.0342	23.1954	0.0256
HHc5+0	0.1192	0.1033	0.1033	0.1338	0.1191	0.1191	−13.3203	0.0227	−10.9428	0.0193
HHc5+1	0.0986	0.0858	0.0858	0.1169	0.1052	0.1052	−12.9592	0.0275	−9.9974	0.0211
HHc5+2	0.1023	0.0860	0.0861	0.1187	0.1033	0.1033	−15.8877	0.0283	−12.9364	0.0214
HHc5+3	0.0866	0.0743	0.0743	0.1054	0.0942	0.0942	−14.1943	0.0308	−10.5845	0.0229
HHc5+4	0.0870	0.0732	0.0732	0.1067	0.0929	0.0929	−15.9044	0.0339	−12.9140	0.0224
HHc5+5	0.0904	0.0784	0.0784	0.1103	0.0988	0.0988	−13.2834	0.0349	−10.4236	0.0221
HHc6+0	0.1167	0.0648	0.0648	0.1326	0.0865	0.0865	−44.4823	−0.0021	−34.7968	−0.0016
HHc6+1	0.1171	0.0625	0.0625	0.1312	0.0845	0.0845	−46.6141	−0.0035	−35.6037	−0.0017
HHc6+2	0.1005	0.0626	0.0626	0.1212	0.0823	0.0823	−37.7607	0.0025	−32.1078	−0.0020
HHc6+3	0.1139	0.0728	0.0728	0.1336	0.0910	0.0910	−36.1434	−0.0016	−31.8518	−0.0033
HHc6+4	0.1069	0.0650	0.0650	0.1277	0.0848	0.0848	−39.1987	−0.0033	−33.6261	−0.0054
HHc6+5	0.0914	0.0559	0.0559	0.1139	0.0738	0.0738	−38.9038	−0.0020	−35.2514	−0.0045
HHc9+0	0.2578	0.0861	0.0859	0.2692	0.1001	0.1000	−66.6543	−0.1503	−62.8665	−0.0890
HHc9+1	0.2158	0.0807	0.0806	0.2324	0.0962	0.0962	−62.6309	−0.0727	−58.5991	−0.0134
HHc9+2	0.2479	0.0796	0.0795	0.2584	0.0953	0.0953	−67.9262	−0.1194	−63.1230	−0.0627
HHc9+3	0.2155	0.0907	0.0907	0.2350	0.1077	0.1077	−57.9252	−0.0298	−54.1639	0.0058
HHc9+4	0.2288	0.0698	0.0697	0.2396	0.0870	0.0870	−69.5279	−0.0660	−63.6876	−0.0257
HHc9+5	0.2288	0.0688	0.0687	0.2337	0.0810	0.0810	−69.9580	−0.0313	−65.3429	−0.0226

NOTES: This table reports MAE and RMSE by contract + offset-tick under global calibration (Method 0), alongside percentage changes of CS+H relative to Bla76 and CS99b. Note that there is no HHc1 + 0 because there is no data with those requeriments.

Table 16: Errors in the approximation analysis.

Contract	MAE			RMSE			Δ MAE (%)		Δ RMSE (%)	
	Bla76	CS99b	CS+H	Bla76	CS99b	CS+H	vs Bla76	vs CS99b	vs Bla76	vs CS99b
HHc2 + 0	0.0558	0.0541	0.0537	0.0973	0.0939	0.0935	−3.8115	−0.6867	−3.8628	−0.3860
HHc3 + 0	0.0540	0.0530	0.0529	0.0999	0.0991	0.0994	−2.170	−0.1759	−0.4951	0.3407
HHc3 + 1	0.0522	0.0470	0.0461	0.1013	0.0920	0.0898	−11.7719	−1.9271	−11.4028	−2.4589
HHc3 + 2	0.0512	0.0468	0.0457	0.1044	0.0965	0.0951	−10.8329	−2.3026	−8.9181	−1.4574

NOTES: This table reports, for each contract + offset-tick, the error metrics MAE and RMSE under the three models (Bla76, CS99b, CS+H) in the Greeks-based approximation analysis, together with percentage changes of CS+H relative to Bla76 and CS99b.

Figure 1: Empirical evidence of a "hump-shaped" volatility structure.

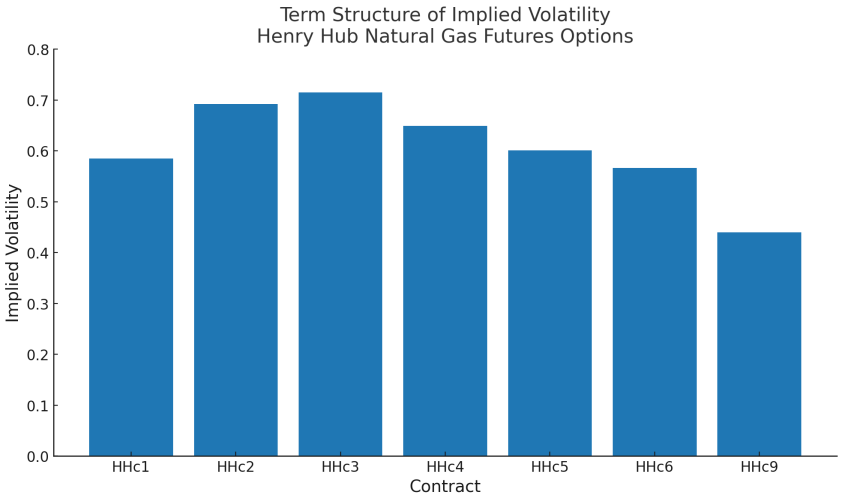

NOTES: This figure provides empirical evidence of a hump-shaped volatility term-structure in HH contracts. Values have been obtained by calibrating Bla76 volatilities by contract over the period January 2, 2020 to May 30, 2025.

Figure 2: Seasonality in monthly natural gas futures contracts.

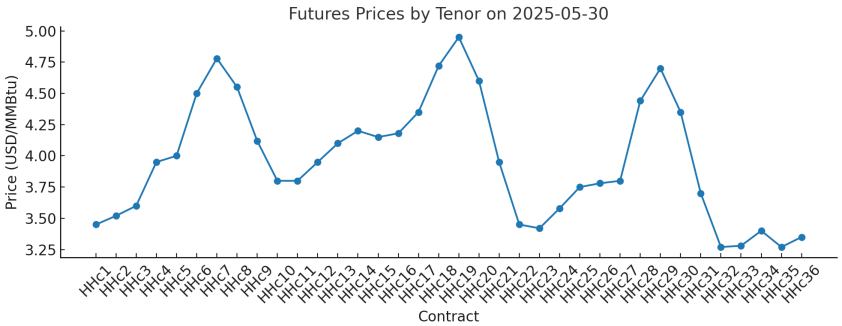

NOTES: The chart highlights the systematic seasonal fluctuations of HH prices, reflecting higher demand (and thus prices) during the winter season and lower levels in the summer months. These values correspond to May 30, 2025.

Figure 3: Evidence of mean-reversion in natural gas futures.

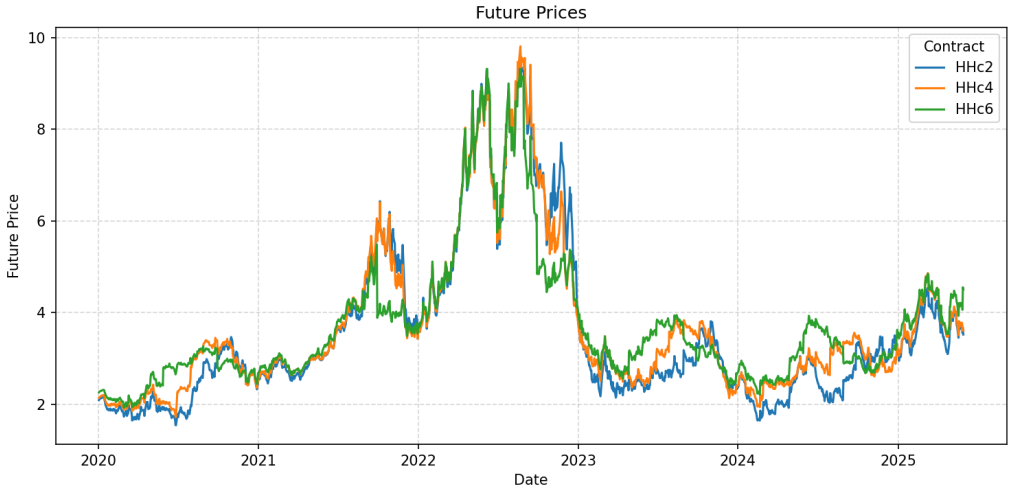

NOTES: This figure depicts the mean-reversion behavior of HH natural gas prices. Temporary deviations above or below the long-term equilibrium price are followed by corrective movements back toward the historical average, consistent with a mean-reverting stochastic process. For this example, we use the HHc2, HHc4, and HHc6 contract.

Figure 4: Samuelson effect: volatility term-structure in natural gas futures.

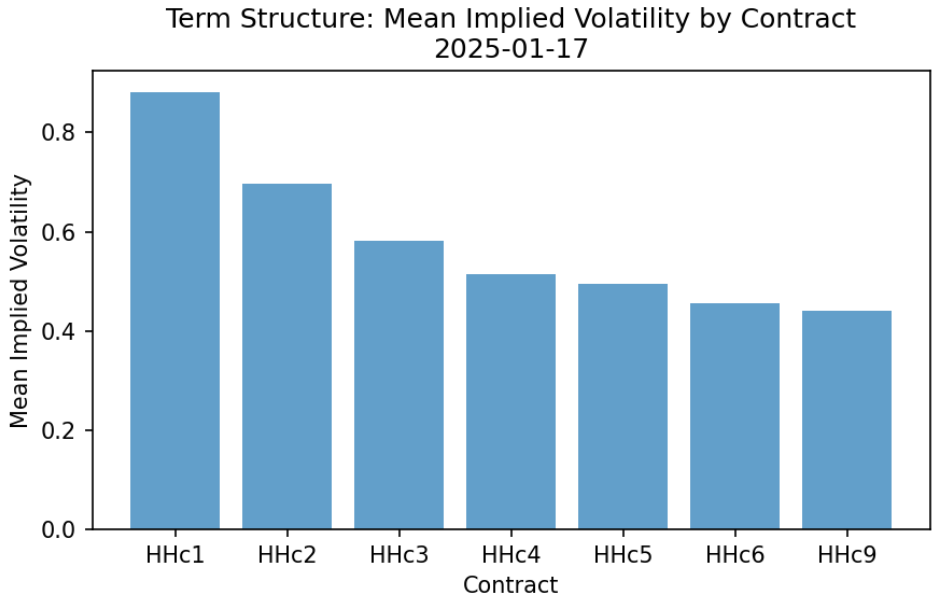

NOTES: This figure illustrates the Samuelson effect in HH futures. Values have been obtained by averaging option implied Bla76 volatilities of contracts HHc1 through HHc9 on January 17, 2025.

Figure 5: Hump effect: volatility term-structure in natural gas futures.

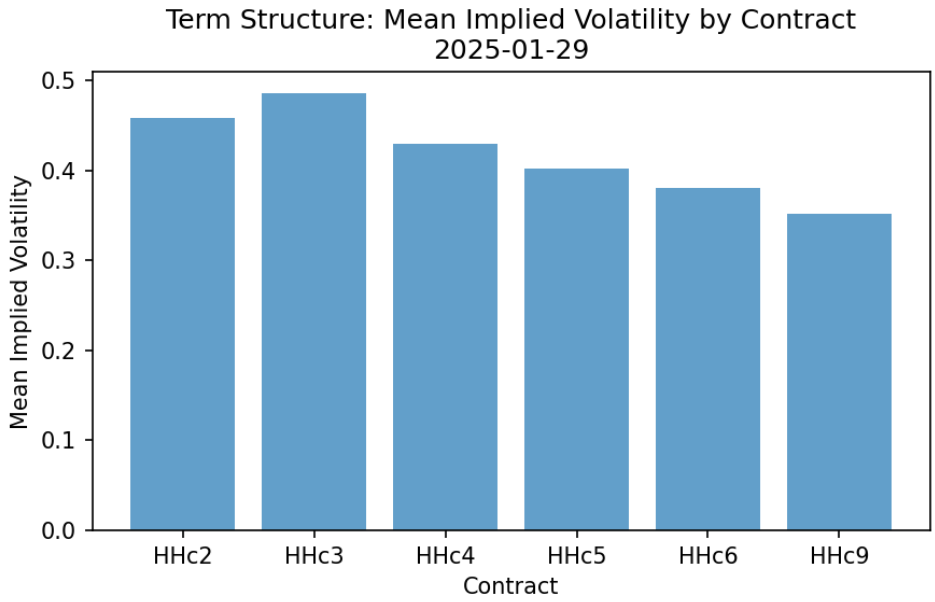

NOTES: This figure illustrates the Humps effect in HH option contracts. Values have been obtained by averaging option implied Bla76 volatilities of contracts HHc1 through HHc9 on January 29, 2025.

Figure 6: Option prices.

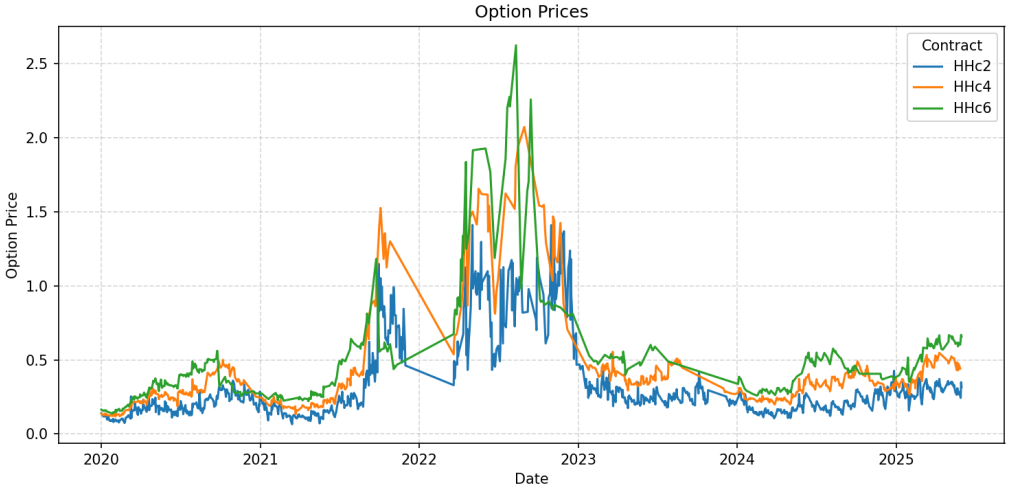

NOTES: This figure illustrates the historical evolution of option prices on HHc2, HHc4, and HHc6 contract at offset-tick 0, over our sample period.

Figure 7: Historical MAE for model calibration.

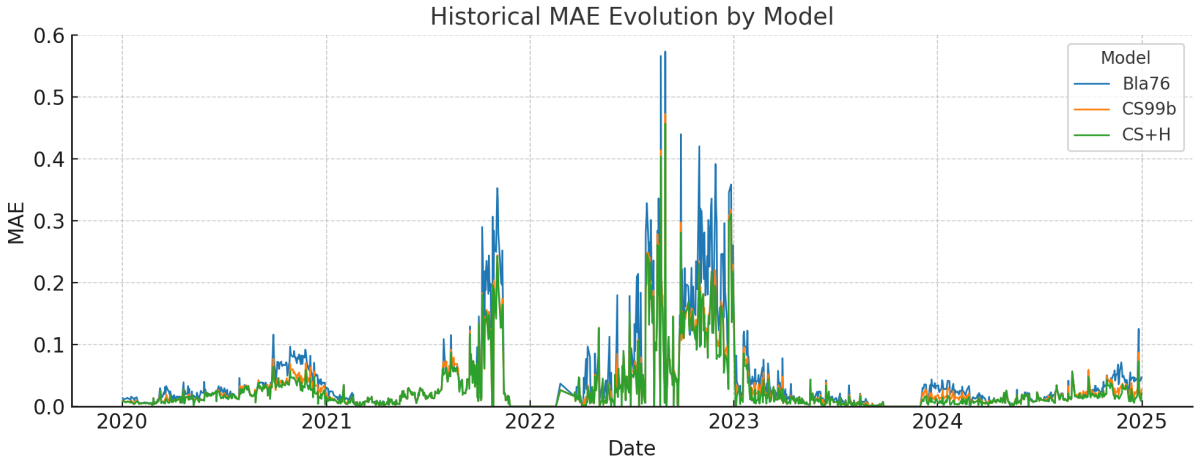

(a) Method 1

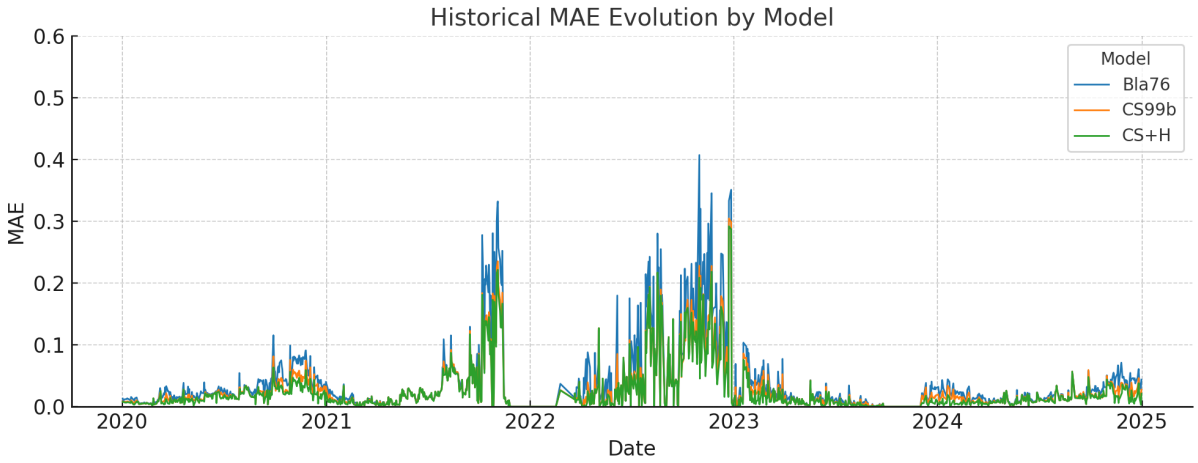

(b) Method 2

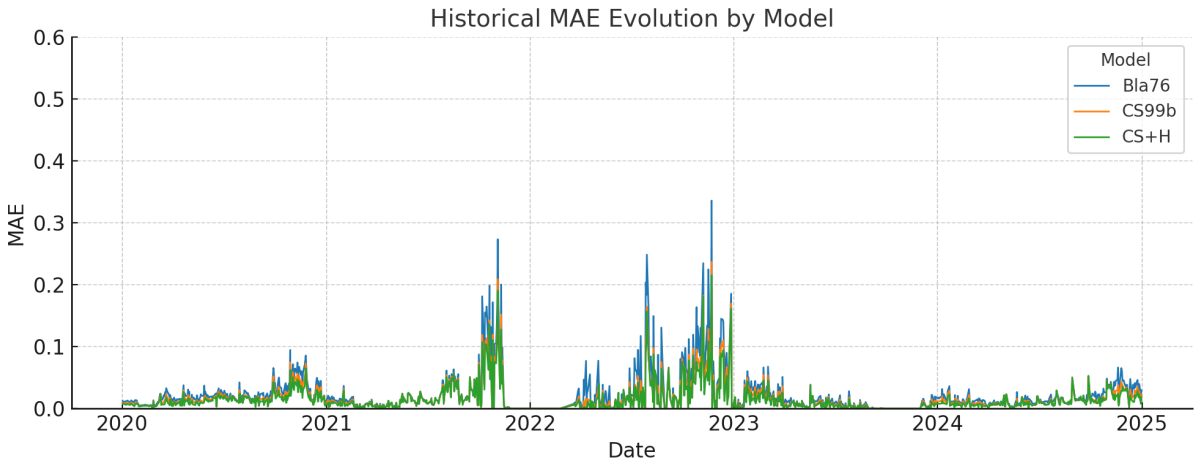

(c) Method 3

NOTES: This figure displays the historical evolution of in-sample calibration MAE for three models (Bla76, CS99b, CS+H). Subfigures (a), (b), and (c) correspond to Method 1 (by date), Method 2 (by date and moneyness), and Method 3 (by date and offset-tick bucket), respectively.

Figure 8: Historical RMSE for model calibration.

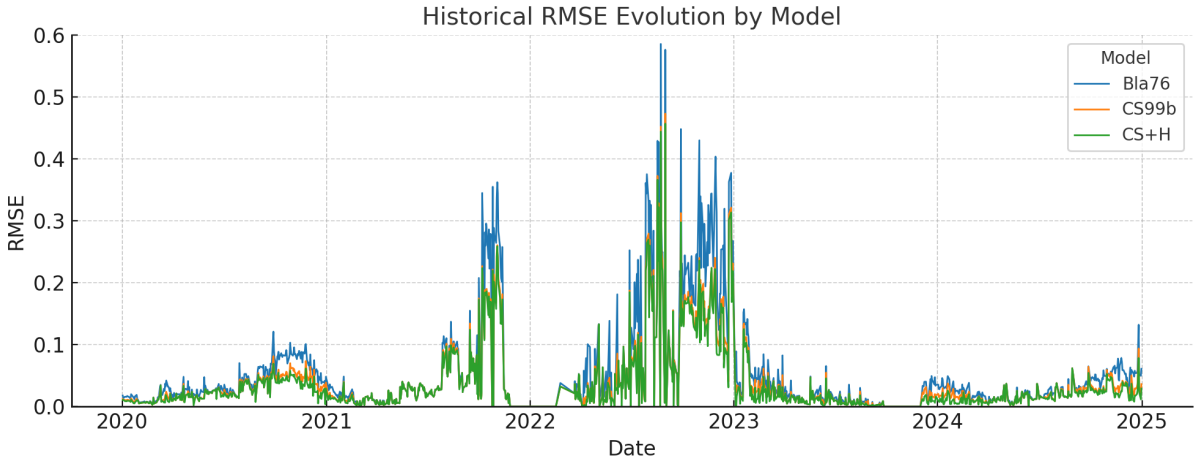

(a) Method 1

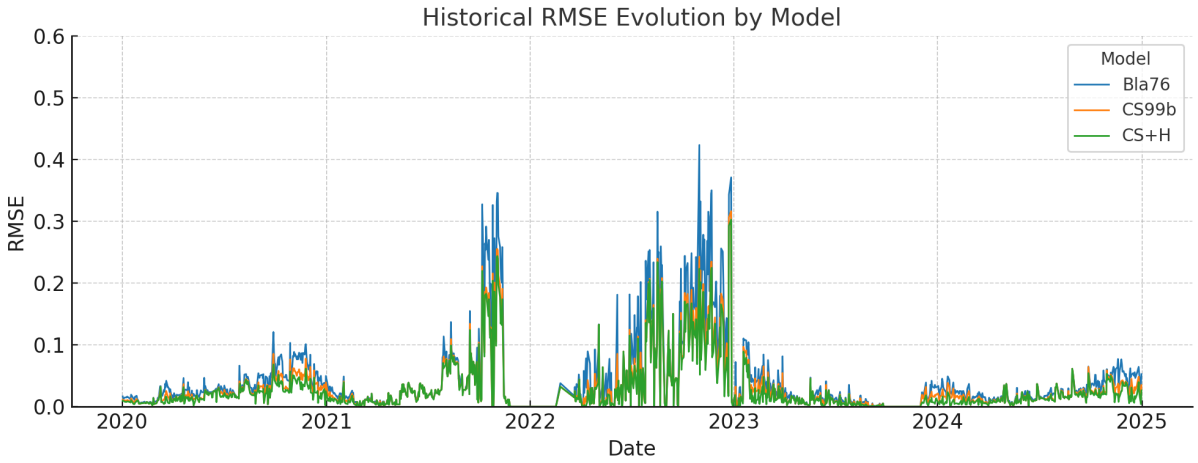

(b) Method 2

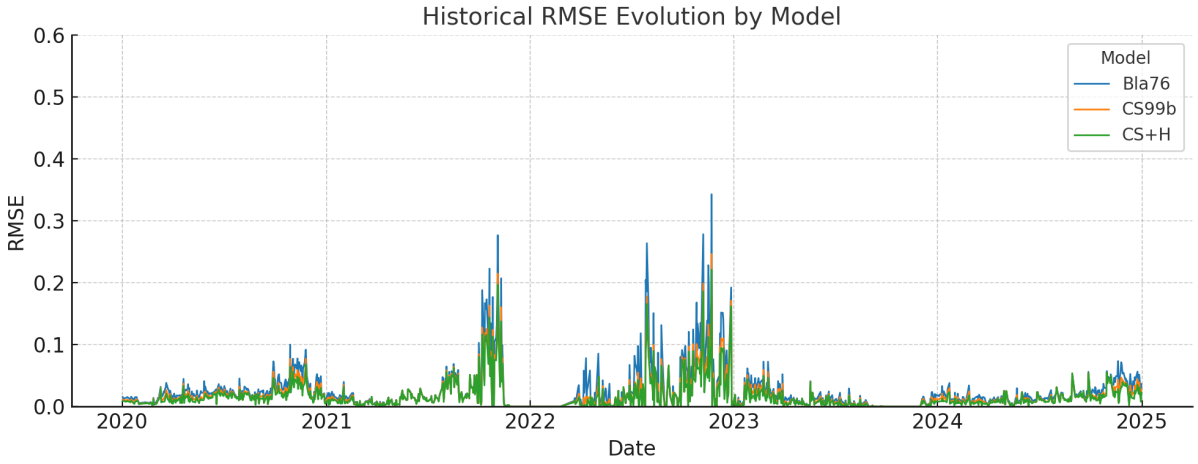

(c) Method 3

NOTES: This figure displays the historical evolution of in-sample calibration RMSE for three models (Bla76, CS99b, CS+H). Subfigures (a), (b), and (c) correspond to Method 1 (by date), Method 2 (by date and moneyness), and Method 3 (by date and offset-tick bucket), respectively.

Figure 9: Volatility term-structures under calibration Methods 0 and 1.

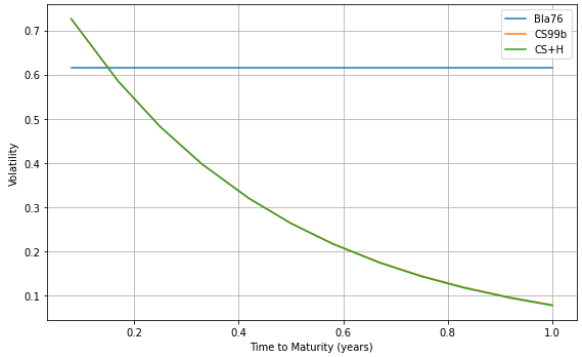

(a) Method 0

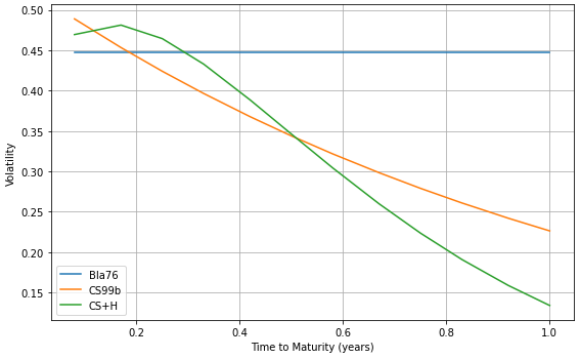

(b) Method 1 (August 14, 2020)

NOTES: Subfigure (a) shows the volatility term-structures for the three models (Bla76, CS99b, and CS+H) using parameters obtained under Method 0. CS99b is not visible because its curve overlaps with CS+H. Subfigure (b) shows the term-structures using parameters calibrated on August 14, 2020, under Method 1.

Figure 10: Volatility term-structures under calibration Method 2.

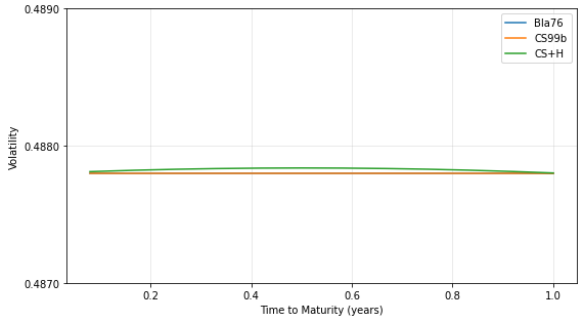

(a) ATM bucket

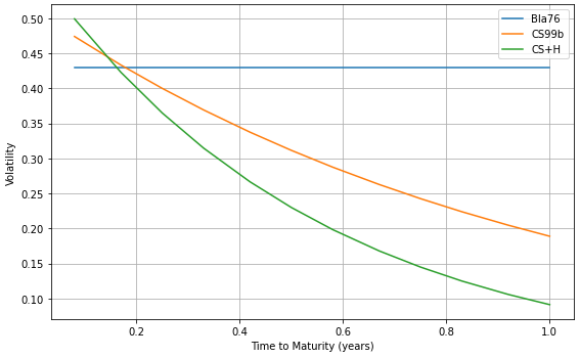

(b) OTM bucket

NOTES: This figure shows the term-structures of volatility for the three pricing models (Bla76, CS99b, CS+H) using parameters calibrated on August 14, 2020, under Method 2. Subfigure (a) displays the results for the ATM moneyness bucket, whereas subfigure (b) shows the OTM bucket. In Subfigure (a) the three curves overlap.

Figure 11: volatility term-structures under calibration Method 3.

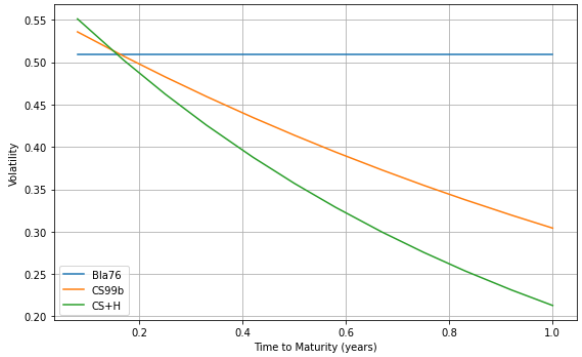

(a) Offset-Tick 0

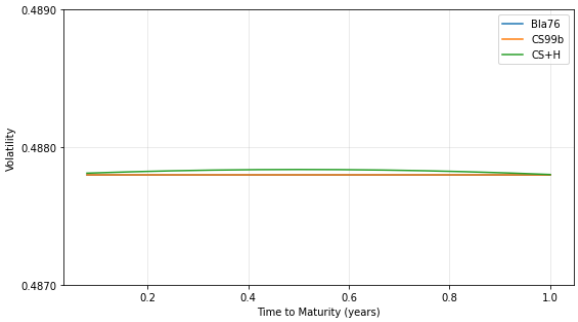

(b) Offset-Tick 1

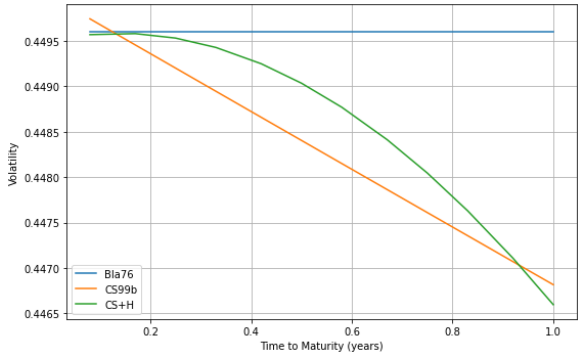

(c) Offset-Tick 2

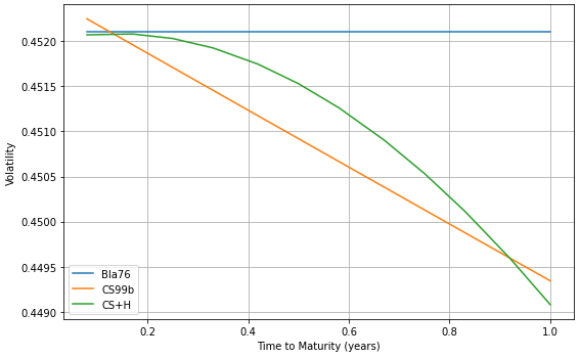

(d) Offset-Tick 3

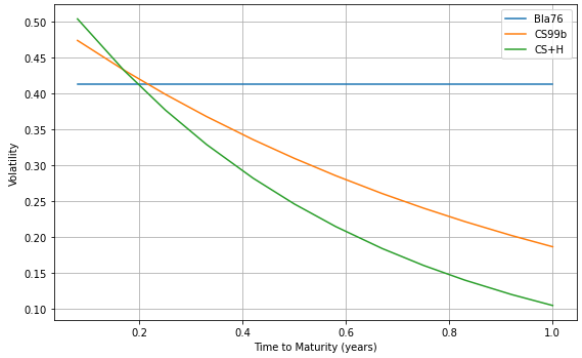

(e) Offset-Tick 4

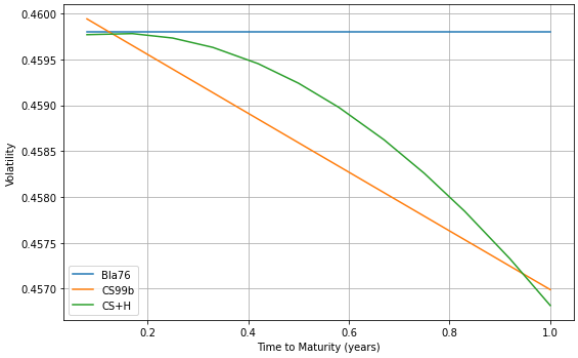

(f) Offset-Tick 5

NOTES: These panels display the volatility term-structures for the three models (Bla76, CS99b, CS+H) using parameters calibrated on August 14, 2020 under Method 3, for each offset-tick bucket from 0 through 5. In Panel (b) the three curves overlap.

Figure 12: Historical approximation error – Contract HHc3.

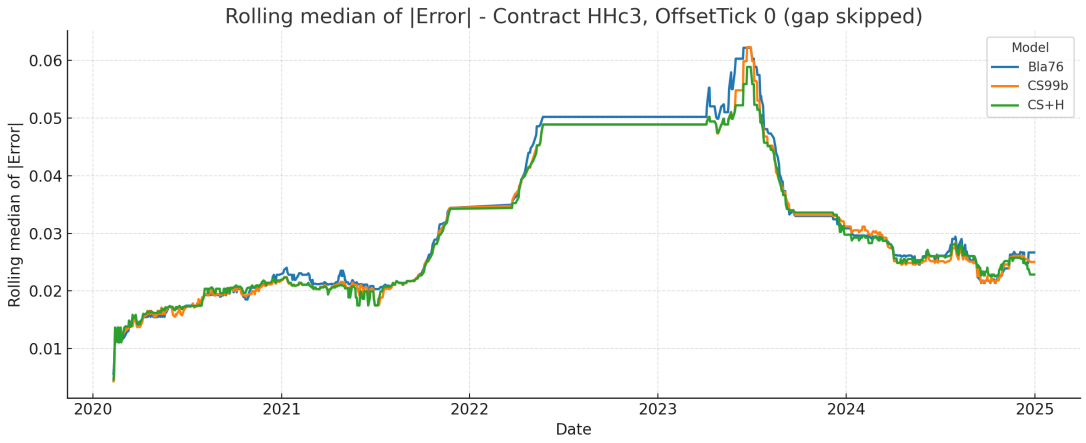

(a) HHc3+0

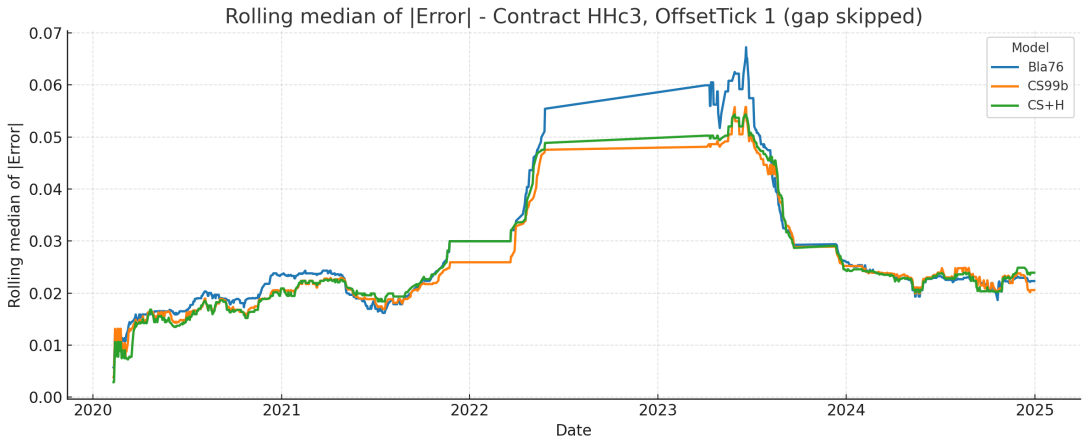

(b) HHc3+1

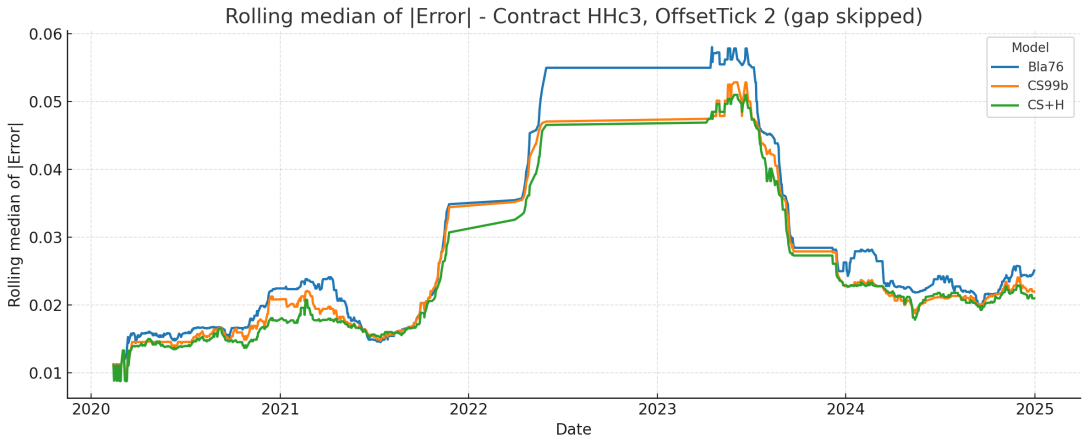

(c) HHc3+2

NOTES: This figure displays the historical evolution of the approximation error for the three models (Bla76, CS99b, and CS+H). Subfigures (a), (b), and (c) correspond to HHc3+0, HHc3+1, and HHc3+2, respectively. Each curve is the trailing 120-observation rolling median of the absolute approximation error. We remove the interval 2022-06-01 to 2023-03-31 where option quotes are largely missing; the plots show an explicit gap there rather than inflated errors.

B Appendix B: Proofs for CS+H

B.1 Proof of the Spot Price SDE

We start from the SDE

$$\frac{dF(t,T)}{F(t,T)} = \sigma(t,T)\,dW_t,$$

where

$$\sigma(t,T) = \big(\sigma + \kappa(T-t)\big)\,e^{-\alpha(T-t)}.$$

Applying Itô's Lemma and subsequently integrating from 0 to t, we obtain

$$F(t,T) = F(0,T)\,\exp\Big\{\int_0^t \sigma(u,T)\,\mathrm{d}W_u \;-\; \tfrac{1}{2}\int_0^t \sigma(u,T)^2\,\mathrm{d}u\Big\}. \tag{B.1}$$

We know that when $T \to t$ the futures converges to the spot. Therefore,

$$F(t,t) = S(t) = F(0,t)\,\exp\Big\{\int_0^t \sigma(u,t)\,\mathrm{d}W_u \;-\; \tfrac{1}{2}\int_0^t \sigma(u,t)^2\,\mathrm{d}u\Big\}. \tag{B.2}$$

Differentiating both sides with respect to t, and rearranging terms, we obtain

$$\frac{\mathrm{d}S(t)}{S(t)} = \Big(\frac{\partial \ln F(0,t)}{\partial t} - \int_0^t \sigma(u,t)\,\frac{\partial \sigma(u,t)}{\partial t}\,\mathrm{d}u + \int_0^t \frac{\partial \sigma(u,t)}{\partial t}\,\mathrm{d}W_u\Big)\mathrm{d}t + \sigma(t,t)\,\mathrm{d}W_t. \tag{B.3}$$

Since $M = e^{-2\alpha(T-t)}$, we rewrite $\sigma(t,T)$ as

$$\sigma(t,T) = \big(\sigma + \kappa(T-t)\big)\,\sqrt{M}.$$

Then the partial derivative with respect to T is

$$\frac{\partial \sigma(t,T)}{\partial T} = \frac{\partial}{\partial T}\Big(\big(\sigma + \kappa(T-t)\big)\,\sqrt{M} = \sqrt{M}\big(-\alpha\,\sigma + \kappa - \alpha\,\kappa(T-t)\big),$$

which simplifies to

$$\frac{\partial \sigma(t,T)}{\partial T} = \sqrt{M}\Big(\kappa - \alpha\big(\sigma + \kappa(T-t)\big)\Big).$$

To simplify notation, define

$$\frac{dS(t)}{S(t)} = y(t)dt + \sigma(t,t)dW_t,$$

where

$$y(t) = \frac{\partial \ln F(0,t)}{\partial t} - \int_0^t \sigma(u,t)\frac{\partial \sigma(u,t)}{\partial t}du + \int_0^t \frac{\partial \sigma(u,t)}{\partial t}dW_u.$$

If we substitute the explicit form of $\sigma(u,t)$, we obtain

$$y(t) = \frac{\partial}{\partial t}\ln F(0,t) - \int_0^t M(u,t)\big(\sigma + k\,(t-u)\big)\Big(\kappa - \alpha\left(\sigma + \kappa\,(t-u)\right)\Big)\,\mathrm{d}u + \int_0^t \sqrt{M(u,t)}\Big(\kappa - \alpha\left(\sigma + \kappa\,(t-u)\right)\Big)\,\mathrm{d}W_u.$$

Expanding the product inside the deterministic integral

$$M(u,t)\big(\sigma+\kappa\,(t-u)\big)\Big(\kappa-\alpha\left(\sigma+\kappa\,(t-u)\right)\Big) = M(u,t)\Big(\sigma\kappa+\kappa^2\,(t-u)-\alpha\left(\sigma+\kappa\,(t-u)\right)^2\Big)$$

$$= M(u,t)\Big((\sigma\kappa-\alpha\,\sigma^2)+(\kappa^2-2\,\alpha\,\sigma\kappa)\,(t-u)-\alpha\,\kappa^2\,(t-u)^2\Big).$$

Then $y(t)$ takes the form

$$y(t) = \frac{\partial}{\partial t}\ln F(0,t) - \int_0^t M(u,t)\Big((\sigma\kappa-\alpha\,\sigma^2)+(\kappa^2-2\alpha\,\sigma\kappa)\,(t-u)-\alpha\,\kappa^2\,(t-u)^2\Big)\,\mathrm{d}u + \int_0^t \sqrt{M(u,t)}\Big(\kappa-\alpha\left(\sigma+\kappa\,(t-u)\right)\Big)\,\mathrm{d}W_u\,.$$

If we do the same as in (B.2) but take logarithms, we obtain

$$\ln S(t) = \ln F(0,t) + \int_0^t \left(\sigma+\kappa\,(t-u)\right)\sqrt{M(u,t)}\mathrm{d}W_u - \tfrac{1}{2}\int_0^t \left(\sigma+\kappa\,(t-u)\right)^2 M(u,t)\mathrm{d}u.$$

Note that

$$\int_0^t \left(\sigma+\kappa\,(t-u)\right)\sqrt{M(u,t)}\,\mathrm{d}W_u \quad \text{and} \quad (\kappa-\alpha)\int_0^t \left(\sigma+\kappa\,(t-u)\right)\sqrt{M(u,t)}\,\mathrm{d}W_u,$$

differ only by the constant factor $(\kappa-\alpha)$. Hence

$$(\kappa-\alpha)\int_0^t \left(\sigma+\kappa\,(t-u)\right)\sqrt{M(u,t)}\,\mathrm{d}W_u = (\kappa-\alpha)\Big(\ln S(t) - \ln F(0,t) + \tfrac{1}{2}\int_0^t \left(\sigma+\kappa\,(t-u)\right)^2 M(u,t)\,\mathrm{d}u\Big).$$

Therefore,

$$y(t) = \frac{\partial}{\partial t}\ln F(0,t) - \int_0^t M(u,t)\left((\sigma\kappa-\alpha\,\sigma^2)+(\kappa^2-2\alpha\,\sigma\kappa)\,(t-u)-\alpha\,\kappa^2\,(t-u)^2\right)\mathrm{d}u + (\kappa-\alpha)\Big(\ln S(t) - \ln F(0,t) + \tfrac{1}{2}\int_0^t (\sigma+\kappa\,(t-u))^2 M(u,t)\,\mathrm{d}u\Big). \tag{B.4}$$

We denote the integral above by

$$G = \int_0^t M(u,t)\Big((\sigma\kappa-\alpha\,\sigma^2)+(\kappa^2-2\alpha\,\sigma\kappa)\,(t-u)-\alpha\,\kappa^2\,(t-u)^2\Big)\,\mathrm{d}u.$$

We can separate G into

$$G = (\sigma\kappa - \alpha\sigma^2)\, G_1 + (\kappa^2 - 2\alpha\,\sigma\kappa)\, G_2 - \alpha\,\kappa^2\, G_3, \tag{B.5}$$

where

$$G_1 = \int_0^t M(u,t)\mathrm{d}u, \quad G_2 = \int_0^t M(u,t)(t-u)\,\mathrm{d}u, \quad G_3 = \int_0^t M(u,t)(t-u)^2\,\mathrm{d}u.$$

We solve each integral separately

$$G_1 = \int_0^t M(u,t)\mathrm{d}u = \Big(\frac{1}{2\alpha}M(u,t)\Big)\Big|_{u=0}^{u=t} = \frac{1-M(0,t)}{2\alpha}. \tag{B.6}$$

We compute G_2 by integration by parts

$$G_2 = \int_0^t M(u,t)(t-u)\,\mathrm{d}u.$$

Let $u = t-u$, $\mathrm{d}v = M(u,t)$, so $\mathrm{d}u = -1$ and $v = \frac{1}{2\alpha}M(u,t)$. Then

$$G_2 = \Big((t-u)\,\frac{1}{2\alpha}M(u,t)\Big)\Big|_{u=0}^{u=t} + \int_0^t \frac{1}{2\alpha}M(u,t)\,\mathrm{d}u = \frac{1}{2\alpha}\big(-t\,M(0,t)\big) + \frac{1}{2\alpha}G_1.$$

Hence,

$$G_2 = \frac{1-M(0,t)(1+2\alpha t)}{4\alpha^2}. \tag{B.7}$$

We compute G_3 by integration by parts

$$G_3 = \int_0^t M(u,t)(t-u)^2\,\mathrm{d}u.$$

Let $u = (t-u)^2$, $\mathrm{d}v = M(u,t)$, so that $\mathrm{d}u = -2\,(t-u)$ and $v = \frac{1}{2\alpha}M(u,t)$. Then

$$G_3 = \Big((t-u)^2\,\frac{1}{2\alpha}M(u,t)\Big)\Big|_{u=0}^{u=t} - \int_0^t \tfrac{1}{2\alpha}M(u,t)\big(-2\,(t-u)\big)\,\mathrm{d}u = -\frac{t^2}{2\alpha}M(0,t) + \frac{1}{\alpha}G_2,$$

we conclude that

$$G_3 = \frac{1-M(0,t)\left(1+2\alpha t+2\alpha^2t^2\right)}{4\alpha^3}. \tag{B.8}$$

Substituting (B.6),(B.7) and (B.8) into (B.5) we have:

$$\begin{aligned} G = (\sigma\,\kappa - \alpha\,\sigma^2)\,\frac{1-M(0,t)}{2\alpha} + (\kappa^2 - 2\alpha\,\sigma\,\kappa)\Big(\frac{1-M(0,t)(1+2\alpha t)}{4\alpha^2}\Big) \\ -(\alpha\,\kappa^2)\Big(\frac{1-M(0,t)\left(1+2\alpha t+2\alpha^2t^2\right)}{4\alpha^3}\Big). \end{aligned} \tag{B.9}$$

Substituting (B.9) into (B.4) we have

$$
\begin{aligned}
y(t) = \frac{\partial}{\partial t}\ln F(0,t) - \Bigg(& (\sigma\kappa - \alpha\sigma^2)\,\frac{1-M(0,t)}{2\alpha} + (\kappa^2 - 2\alpha\sigma\kappa)\Big(\frac{1-M(0,t)(1+2\alpha t)}{4\alpha^2}\Big) \\
& - (\alpha\kappa^2)\Big(\frac{1-M(0,t)\left(1+2\alpha t+2\alpha^2 t^2\right)}{4\alpha^3}\Big)\Bigg) \\
& + (\kappa-\alpha)\Big(\ln S(t) - \ln F(0,t) + \frac{1}{2}\underbrace{\int_0^t (\sigma+\kappa(t-u))^2 M(u,t)\mathrm{d}u}_{H}\Big).
\end{aligned}
\tag{B.10}
$$

We solve the integral H

$$
\begin{aligned}
H &\equiv \int_0^t \big(\sigma+\kappa(t-u)\big)^2 M(u,t)\,\mathrm{d}u \\
&= \int_0^t e^{-2\alpha(t-u)}\big(\sigma^2 + 2\sigma\kappa(t-u) + \kappa^2(t-u)^2\big)\,\mathrm{d}u \\
&= \sigma^2 G_1 + 2\sigma\kappa G_2 + \kappa^2 G_3
\end{aligned}
\tag{B.11}
$$

Substituting (B.11) into (B.10) and then into (B.3) we have

$$
\begin{aligned}
\frac{dS(t)}{S(t)} = \Bigg(& \frac{\partial}{\partial t}\ln F(0,t) - \Big((\sigma\kappa - \alpha\sigma^2)\,\frac{1-M(0,t)}{2\alpha} + (\kappa^2 - 2\alpha\sigma\kappa)\Big(\frac{1-M(0,t)(1+2\alpha t)}{4\alpha^2}\Big) \\
& - \alpha\kappa^2\Big(\frac{1-M(0,t)\left(1+2\alpha t+2\alpha^2 t^2\right)}{4\alpha^3}\Big)\Big) \\
& + (\kappa-\alpha)\Bigg(\ln S(t) - \ln F(0,t) + \frac{1}{2}\Big(\sigma^2\,\frac{1-M(0,t)}{2\alpha} + 2\sigma\kappa\big(\frac{1-M(0,t)(1+2\alpha t)}{4\alpha^2}\big) \\
& + \kappa^2\big(\frac{1-M(0,t)\left(1+2\alpha t+2\alpha^2 t^2\right)}{4\alpha^3}\big)\Big)\Bigg)\Bigg)\,dt + \sigma\,dW_t\,.
\end{aligned}
$$

B.2 Proof of the Futures Curve

Starting from

$$
\frac{dF(t,T)}{F(t,T)} = \big(\sigma+\kappa(T-t)\big)\sqrt{M}\,dW_t.
$$

From Section B.1 we obtained

$$
F(t,t) = S(t) = F(0,t)\exp\Big\{\int_0^t \sigma(u,t)\,\mathrm{d}W_u \;-\; \tfrac{1}{2}\int_0^t \sigma(u,t)^2\,\mathrm{d}u\Big\}. \tag{B.12}
$$

Assuming $\sigma(u,T) = (\sigma + \kappa(T-u))\sqrt{M(u,T)}$. We substitute $\sigma(u,t)$ into (B.12) and we obtain

$$S(t) = F(0,t)\exp\left\{\int_0^t \big(\sigma + \kappa(t-u)\big)\sqrt{M(u,t)}\,\mathrm{d}W_u \;-\; \tfrac{1}{2}\int_0^t \big(\sigma + \kappa(t-u)\big)^2 M(u,t)\,\mathrm{d}u\right\}.$$

Take logarithms

$$\ln S(t) = \ln F(0,t) + \int_0^t \big(\sigma + \kappa(t-u)\big)\sqrt{M(u,t)}\,\mathrm{d}W_u - \underbrace{\tfrac{1}{2}\int_0^t \big(\sigma + \kappa(t-u)\big)^2 M(u,t)\,\mathrm{d}u}_{H}. \tag{B.13}$$

Substitute the closed-form of H into (B.13) and obtain

$$\begin{aligned}\ln S(t) = \ln F(0,t) &+ \int_0^t \big(\sigma + \kappa(t-u)\big)\sqrt{M(u,t)}\,\mathrm{d}W_u \\ &- \frac{1}{2}\left(\sigma^2\Big(\frac{1-M(0,t)}{2\alpha}\Big) + 2\,\sigma\,\kappa\Big(\frac{1-M(0,t)(1+2\alpha t)}{4\alpha^2}\Big)\right. \\ &\left. + \kappa^2\Big(\frac{1-M(0,t)\left(1+2\alpha t+2\alpha^2 t^2\right)}{4\alpha^3}\Big)\right).\end{aligned}$$

Rearranging

$$\begin{aligned}\int_0^t \big(\sigma + \kappa(t-u)\big)\sqrt{M(u,t)}\,\mathrm{d}W_u = \ln\Big(\frac{S(t)}{F(0,t)}\Big) + \frac{1}{2}\left(\sigma^2\,\frac{1-M(0,t)}{2\alpha} + 2\,\sigma\,\kappa\Big(\frac{1-M(0,t)(1+2\alpha t)}{4\alpha^2}\Big)\right. \\ \left. + \kappa^2\Big(\frac{1-M(0,t)\left(1+2\alpha t+2\alpha^2 t^2\right)}{4\alpha^3}\Big)\right).\end{aligned} \tag{B.14}$$

Now we deal with the integral

$$\int_0^t \big(\sigma + \kappa(T-u)\big)\sqrt{M(u,T)}\,\mathrm{d}W_u,$$

which can be written as:

$$\int_0^t \big(\sigma + \kappa(T-u)\big)\,e^{-\alpha T}\,e^{\alpha u}\,\mathrm{d}W_u \;=\; e^{-\alpha T}\int_0^t \big(\sigma + \kappa(T-u)\big)\,e^{\alpha u}\,\mathrm{d}W_u.$$

Using the identity

$$e^{\alpha u} = e^{\alpha u - \alpha t + \alpha t} = e^{-\alpha(t-u)}\,e^{\alpha t} = \sqrt{M(u,t)}\,e^{\alpha t},$$

we obtain

$$e^{-\alpha T}\int_0^t \big(\sigma + \kappa(T-u)\big)\sqrt{M(u,t)}\,e^{\alpha t}\,\mathrm{d}W_u = e^{-\alpha T}\,e^{\alpha t}\int_0^t \big(\sigma + \kappa(T-u)\big)\sqrt{M(u,t)}\,\mathrm{d}W_u.$$

Therefore

$$\int_0^t \big(\sigma+\kappa(T-u)\big)\sqrt{M(u,T)}\,\mathrm{d}W_u = \sqrt{M}\int_0^t \big(\sigma+\kappa(T-u)\big)\sqrt{M(u,t)}\,\mathrm{d}W_u.$$

Now we multiply and divide by $\sigma+\kappa(t-u)$:

$$\int_0^t \big(\sigma+\kappa(T-u)\big)\sqrt{M(u,T)}\,\mathrm{d}W_u = \sqrt{M}\int_0^t \frac{\big(\sigma+\kappa(T-u)\big)\big(\sigma+\kappa(t-u)\big)}{\big(\sigma+\kappa(t-u)\big)}\sqrt{M(u,t)}\,\mathrm{d}W_u.$$

Observe that

$$\sigma+\kappa(T-u)-\big(\sigma+\kappa(t-u)\big) = \kappa(T-u)-\kappa(t-u) = \kappa(T-t).$$

Hence

$$\frac{\sigma+\kappa(T-u)}{\sigma+\kappa(t-u)} = \frac{\sigma+\kappa(t-u)}{\sigma+\kappa(t-u)} + \frac{\kappa(T-t)}{\sigma+\kappa(t-u)} = 1+\frac{\kappa(T-t)}{\sigma+\kappa(t-u)}.$$

Therefore we obtain

$$\begin{aligned}\int_0^t \big(\sigma+\kappa(T-u)\big)\sqrt{M(u,T)}\,\mathrm{d}W_u = \sqrt{M}\int_0^t \big(\sigma+\kappa(t-u)\big)\sqrt{M(u,t)}\,\mathrm{d}W_u \\ +\sqrt{M}\,\kappa(T-t)\int_0^t \sqrt{M(u,t)}\,\mathrm{d}W_u.\end{aligned}$$

If we substitute from equation (B.14), we obtain

$$\begin{aligned}\int_0^t \big(\sigma+\kappa(T-u)\big)\sqrt{M(u,T)}\,\mathrm{d}W_u = \sqrt{M}\,\kappa(T-t)\int_0^t \sqrt{M(u,t)}\,\mathrm{d}W_u + \sqrt{M} \\ \times\left(\ln\frac{S(t)}{F(0,t)} + \frac{1}{2}\left(\sigma^2\,\frac{1-M(0,t)}{2\alpha} + 2\sigma\kappa\Big(\frac{1-M(0,t)(1+2\alpha t)}{4\alpha^2}\Big)\right.\right. \\ \left.\left. +\kappa^2\Big(\frac{1-M(0,t)\big(1+2\alpha t+2\alpha^2t^2\big)}{4\alpha^3}\Big)\right)\right).\end{aligned} \tag{B.15}$$

After substituting (B.15) into equation (B.1) and rearranging, we arrive at the following more compact form for the futures curve at date t

$$F(t,T) = F(0,T)\exp\underbrace{\left\{\sqrt{M}\ln\Big(\frac{S(t)}{F(0,t)}\Big) - \tfrac{\sigma^2}{4\alpha}\sqrt{M(0,T)}\big(e^{2\alpha t}-1\big)\big(\sqrt{M(0,T)}-\sqrt{M(0,t)}\big)\right\}}_{\text{CS99b}}$$
$$\times\exp\left\{\sqrt{M}\,\kappa(T-t)\int_0^t\sqrt{M(u,t)}\,\mathrm{d}W_u + \tfrac{1}{2}\big(\sqrt{M}-1\big)V^2(0,t)\right\}.$$

B.3 Futures Price Derivation

We define the futures price under the risk-neutral measure Q by

$$F(t,T) \;=\; \mathbb{E}_t^Q\big[F(T,T)\big] = \;\mathbb{E}_t^Q\big[S(T)\big].$$

Applying Itô's lemma to the process $f(t) = \ln F(t,T)$, note that

$$f_F = \frac{1}{F(t,T)}, \qquad f_{FF} = -\frac{1}{F^2(t,T)}, \qquad f_t = 0.$$

Hence

$$d\big[\ln F(t,T)\big] = \frac{1}{F(t,T)}\,dF(t,T) - \frac{1}{2}\,\frac{1}{F(t,T)^2}\,\big(dF(t,T)\big)^2. \tag{B.16}$$

Under the model

$$\frac{dF(t,T)}{F(t,T)} = \big(\sigma + \kappa\,(T-t)\big)\,\sqrt{M}\,dW_t,$$

we have

$$\begin{aligned}\ln F(T,T) - \ln F(t,T) = -\tfrac{1}{2}\int_t^T M(s,T)\big(\sigma^2 + 2\,\sigma\,\kappa\,(T-s) + \kappa^2\,(T-s)^2\big)\,\mathrm{d}s \\ + \int_t^T \big(\sigma + \kappa\,(T-s)\big)\,\sqrt{M(s,T)}\,\mathrm{d}W_s.\end{aligned}$$

Substituting into (B.16) gives

$$d\ln F(t,T) = -\frac{1}{2}M\Big(\sigma^2 + 2\,\sigma\,\kappa\,(T-t) + \kappa^2\,(T-t)^2\Big)\,dt + \Big(\sigma + \kappa\,(T-t)\Big)\,\sqrt{M}\,dW_t\,.$$

Integrating both sides from t to T yields

$$\begin{aligned}\ln F(T,T) - \ln F(t,T) = -\frac{1}{2}\int_t^T M(s,T)\Big(\sigma^2 + 2\,\sigma\,\kappa\,(T-s) + \kappa^2\,(T-s)^2\Big)\,\mathrm{d}s \\ + \int_t^T \big(\sigma + \kappa\,(T-s)\big)\,\sqrt{M(s,T)}\,\mathrm{d}W_s.\end{aligned}$$

Rearranging:

$$\begin{aligned}\ln F(T,T) = \ln F(t,T) - \frac{1}{2}\int_t^T M(s,T)\Big(\sigma^2 + 2\,\sigma\,\kappa\,(T-s) + \kappa^2\,(T-s)^2\Big)\,\mathrm{d}s \\ + \int_t^T \big(\sigma + \kappa\,(T-s)\big)\,\sqrt{M(s,T)}\,\mathrm{d}W_s.\end{aligned} \tag{B.17}$$

Provided that $\ln F(t,T)$ is $\mathscr{F}_t$-measurable and the Itô integral has zero mean, we take the conditional expectations $\mathbb{E}_t^Q[\cdot]$ and obtain

$$\mathbb{E}_t^Q\big[\ln F(T,T)\big] = \ln F(t,T) - \tfrac{1}{2}\int_t^T M(s,T)\Big(\sigma^2 + 2\,\sigma\,\kappa\,(T-s) + \kappa^2\,(T-s)^2\Big)\,\mathrm{d}s.$$

We denote the integral above by

$$V^2 = \int_t^T M(s,T)\Big(\sigma^2 + 2\,\sigma\,\kappa\,(T-s) + \kappa^2\,(T-s)^2\Big)\,\mathrm{d}s.$$

We can separate V^2 into the sum of integrals

$$\begin{aligned} V^2 &= \int_t^T M(s,T)\sigma^2\,\mathrm{d}s + 2\int_t^T M(s,T)\sigma\,\kappa\,(T-s)\,\mathrm{d}s + \int_t^T M(s,T)\kappa^2\,(T-s)^2\,\mathrm{d}s \\ &= \sigma^2 \underbrace{\int_t^T M(s,T)\mathrm{d}s}_{V_1^2} + 2\,\sigma\,\kappa \underbrace{\int_t^T M(s,T)(T-s)\,\mathrm{d}s}_{V_2^2} + \kappa^2 \underbrace{\int_t^T M(s,T)(T-s)^2\,\mathrm{d}s}_{V_3^2}. \end{aligned}$$

Therefore,

$$V^2 = \sigma^2 V_1^2 \;+\; 2\,\sigma\,\kappa V_2^2 \;+\; \kappa^2 V_3^2. \tag{B.18}$$

We solve each integral separately

$$V_1^2 = \int_t^T M(s,T)\mathrm{d}s = \Big(-\frac{1}{2\alpha}M(s,T)\Big)\Big|_{s=t}^{s=T} = \frac{1}{2\alpha}(1-M).$$

Compute V_2^2 by integration by parts

$$V_2^2 = \int_t^T M(s,T)(T-s)\,\mathrm{d}s.$$

Let $u = T-s$, $\mathrm{d}v = M(s,T)\mathrm{d}s$, so $\mathrm{d}u = -\mathrm{d}s$ and $v = \frac{1}{2\alpha}M(s,T)$. Then

$$\begin{aligned} V_2^2 &= \Big((T-s)\,\frac{1}{2\alpha}e^{-2\alpha\,(T-s)}M(s,T)\Big)\Big|_{s=t}^{s=T} + \tfrac{1}{2\alpha}\int_t^T M(s,T)\,\mathrm{d}s \\ &= -\frac{T-t}{2\alpha}M + \frac{1}{2\alpha}V_1^2 = -\frac{T-t}{2\alpha}M + \frac{1-M}{4\alpha^2} \\ &= \frac{1-M\big(1+2\alpha(T-t)\big)}{4\alpha^2}. \end{aligned}$$

Compute V_3^2 by integration by parts:

$$V_3^2 = \int_t^T M(s,T)\,(T-s)^2\,\mathrm{d}s.$$

Let $u=(T-s)^2$, $\mathrm{d}v=M(s,T)\,\mathrm{d}s$, so that $\mathrm{d}u=-2\,(T-s)\,\mathrm{d}s$ and $v=\frac{1}{2\alpha}M(s,T)$. Then

$$\begin{aligned}
V_3^2 &= \Big((T-s)^2\,\frac{1}{2\alpha}M(s,T)\Big)\Big|_{s=t}^{s=T} - \int_t^T \frac{1}{2\alpha}M(s,T)\big(-2\,(T-s)\big)\,\mathrm{d}s \\
&= -\frac{(T-t)^2}{2\alpha}\,M + \frac{1}{\alpha}\int_t^T M(s,T)\,(T-s)\,\mathrm{d}s \\
&= -\frac{(T-t)^2}{2\alpha}\,M + \frac{1}{\alpha}\,V_2^2 = -\frac{(T-t)^2}{2\alpha}\,M - \frac{T-t}{2\alpha^2}\,M + \frac{1-M}{4\alpha^3} \\
&= \frac{1-M\big(1+2\alpha(T-t)+2\alpha^2(T-t)^2\big)}{4\alpha^3}.
\end{aligned}$$

Substituting into (B.18) we have

$$V^2=\sigma^2\Big(\frac{1-M}{2\alpha}\Big)+2\,\sigma\,\kappa\Big(\frac{1-M\big(1+2\alpha(T-t)\big)}{4\alpha^2}\Big)+\kappa^2\Big(\frac{1-M\big(1+2\alpha(T-t)+2\alpha^2(T-t)^2\big)}{4\alpha^3}\Big).$$

To write V^2 more compactly:

$$V^2=A(1-M)\;-\;BM,$$

Then,

$$\mathbb{E}_t^Q\big[\ln F(T,T)\big]=\ln F(t,T)-\tfrac{1}{2}\Big(A(1-M)-BM\Big).$$

The only random term in (B.17) is the stochastic integral, its conditional variance $\mathbb{V}_t^Q[\cdot]$ is

$$\mathbb{V}_t^Q\big[\ln F(T,T)\big]=\mathbb{V}_t^Q\Big[\int_t^T(\sigma+\kappa\,(T-s))\,\sqrt{M(s,T)}\,\mathrm{d}W_s\Big]=\int_t^T\big(\sigma+\kappa\,(T-s)\big)^2M(s,T)\mathrm{d}s=V^2.$$

We show that $F(t,T)$ is a Q-martingale by verifying

$$\mathbb{E}_t^Q\big[F(T,T)\big]=F(t,T). \tag{B.19}$$

From (B.17) we have

$$\begin{aligned}
F(T,T)=F(t,T)\,\exp\Big\{&-\tfrac{1}{2}\int_t^T M(s,T)\Big(\sigma^2+2\,\sigma\,\kappa\,(T-s)+\kappa^2\,(T-s)^2\Big)\,\mathrm{d}s \\
&+\int_t^T\big(\sigma+\kappa\,(T-s)\big)\,\sqrt{M(s,T)}\,\mathrm{d}W_s\Big\}.
\end{aligned}$$

Hence,

$$\begin{aligned}
\mathbb{E}_t^Q\big[F(T,T)\big]=F(t,T)\,\mathbb{E}_t^Q\Big[\exp\Big\{&-\tfrac{1}{2}\int_t^T M(s,T)\Big(\sigma^2+2\,\sigma\,\kappa\,(T-s)+\kappa^2\,(T-s)^2\Big)\,\mathrm{d}s \\
&+\int_t^T\Big(\sigma+\kappa\,(T-s)\Big)\,\sqrt{M(s,T)}\,\mathrm{d}W_s\Big\}\Big].
\end{aligned} \tag{B.20}$$

Set

$$X \;=\; \int_t^T \big(\sigma + \kappa\,(T-s)\big)\,\sqrt{M(s,T)}\,\mathrm{d}W_s,$$

so that

$$X \sim \mathcal{N}(0, V^2), \quad V^2 = A(1-M) - B\,M.$$

It follows that

$$\mathbb{E}_t^Q\big[e^X\big] = \exp\big\{\tfrac{1}{2}V^2\big\}. \tag{B.21}$$

Substituting (B.21) and the result of the deterministic integral into (B.20) gives

$$\mathbb{E}_t^Q\big[F(T,T)\big] = F(t,T)\exp\Big\{-\tfrac{1}{2}V^2 + \tfrac{1}{2}V^2\Big\} = F(t,T),$$

which completes the proof of (B.19)

$$F(t,T) \;=\; \mathbb{E}_t^Q\big[F(T,T)\big] \;=\; \mathbb{E}_t^Q\big[S(T)\big],$$

proving that $F(t,T)$ is a martingale.

C Appendix C: Derivation of Greeks

From d_1 we have

$$V\,d_1 = \ln\big(F(t,T)/K\big) + \tfrac{1}{2}V^2, \quad \Longrightarrow \quad F(t,T) = K\exp\{Vd_1 - \tfrac{1}{2}V^2\}.$$

Since $d_2 = d_1 - V$, we have

$$\begin{aligned}\mathcal{N}'(d_2) &= \frac{1}{\sqrt{2\pi}}\exp\big\{-\tfrac{1}{2}(d_1-V)^2\big\} = \frac{1}{\sqrt{2\pi}}\exp\big\{-\tfrac{1}{2}d_1^2 - \tfrac{1}{2}V^2 + d_1V\big\}\\ &= \mathcal{N}'(d_1)\exp\{-\tfrac{1}{2}V^2 + d_1V\} = \mathcal{N}'(d_1)\,\frac{F(t,T)}{K}.\end{aligned}$$

Therefore,

$$K\,\mathcal{N}'(d_2) = F(t,T)\,\mathcal{N}'(d_1). \tag{C.1}$$

C.1 Delta (Δ_c)

We differentiate $c(t)$ with respect to $F(t,T)$

$$\begin{aligned}\Delta_c = \frac{\partial c(t)}{\partial F(t,T)} &= \frac{\partial}{\partial F(t,T)}\Big(e^{-r\,(T-t)}\big(F(t,T)\,\mathcal{N}(d_1) - K\,\mathcal{N}(d_2)\big)\Big)\\ &= e^{-r\,(T-t)}\bigg(\mathcal{N}(d_1) + \frac{1}{F(t,T)\,V}\Big(F(t,T)\,\mathcal{N}'(d_1) - K\,\mathcal{N}'(d_2)\Big)\bigg).\end{aligned}$$

Using relation (C.1), the second term vanishes. Therefore,

$$\Delta_c = e^{-r(T-t)}\mathcal{N}(d_1).$$

C.2 Gamma (Γ_c)

We differentiate Δ_c with respect to $F(t,T)$:

$$\Gamma_c = \frac{\partial \Delta_c}{\partial F(t,T)} = \frac{\partial}{\partial F(t,T)}\left(e^{-r(T-t)}\mathcal{N}(d_1)\right) = \frac{e^{-r(T-t)}\mathcal{N}'(d_1)}{F(t,T)V}.$$

C.3 Vega (ν_c)

Note that under the CS+H specification V itself depends on σ, α, and κ. In practice, we therefore define three separate parameter-Vegas.

C.3.1 Sigma-Vega (ν_c^{σ})

We begin by differentiating V^2 with respect to σ

$$\frac{\partial V^2}{\partial \sigma} = \frac{\partial A}{\partial \sigma}(1-M) - \frac{\partial B}{\partial \sigma}M, \tag{C.2}$$

From the definitions of A and B we compute

$$\frac{\partial A}{\partial \sigma} = \frac{\sigma}{\alpha} + \frac{\kappa}{2\alpha^2}, \quad \frac{\partial B}{\partial \sigma} = \frac{\kappa(T-t)}{\alpha}. \tag{C.3}$$

Substituting (C.3) into (C.2) gives

$$\frac{\partial V^2}{\partial \sigma} = \left(\frac{\sigma}{\alpha} + \frac{\kappa}{2\alpha^2}\right)(1-M) - \frac{\kappa(T-t)}{\alpha}M.$$

Since $\frac{\partial V}{\partial \sigma} = \frac{1}{2V}\frac{\partial V^2}{\partial \sigma}$, we obtain

$$\frac{\partial V}{\partial \sigma} = \frac{1}{2V}\left(\left(\frac{\sigma}{\alpha} + \frac{\kappa}{2\alpha^2}\right)(1-M) - \frac{\kappa(T-t)}{\alpha}M\right).$$

Finally, since $\frac{\partial c}{\partial V} = e^{-r(T-t)}F(t,T)\mathcal{N}'(d_1)$, it follows that

$$\nu_c^{(\sigma)} = e^{-r(T-t)}F(t,T)\mathcal{N}'(d_1)\frac{1}{2V}\left(\left(\frac{\sigma}{\alpha} + \frac{\kappa}{2\alpha^2}\right)(1-M) - \frac{\kappa(T-t)}{\alpha}M\right).$$

C.3.2 Alpha-Vega (v_c^{α})

We differentiate V^2 with respect to α:

$$\frac{\partial V^2}{\partial \alpha} = \frac{\partial}{\partial \alpha}\Big(A(1-M) - BM\Big),$$

Then by the product and chain rules,

$$\frac{\partial V^2}{\partial \alpha} = \frac{\partial A}{\partial \alpha}\big(1-M\big) + A\,\frac{\partial\big(1-M\big)}{\partial \alpha} - \Big(\frac{\partial B}{\partial \alpha}M + B\,\frac{\partial M}{\partial \alpha}\Big).$$

Since

$$\frac{\partial M}{\partial \alpha} = -2\,(T-t)M = -2\,(T-t)M,$$

we obtain

$$\frac{\partial V^2}{\partial \alpha} = \frac{\partial A}{\partial \alpha}\,(1-M) + 2A\,(T-t)M - \frac{\partial B}{\partial \alpha}M + 2B\,(T-t)M. \tag{C.4}$$

Next, from

$$A = \frac{\sigma^2}{2\alpha} + \frac{\sigma\,\kappa}{2\alpha^2} + \frac{\kappa^2}{4\alpha^3}, \quad B = \frac{\sigma\,\kappa\,(T-t)}{\alpha} + \frac{\kappa^2\,(T-t)^2}{2\alpha} + \frac{\kappa^2\,(T-t)}{2\alpha^2},$$

one computes

$$\frac{\partial A}{\partial \alpha} = -\frac{\sigma^2}{2\alpha^2} - \frac{2\,\sigma\,\kappa}{2\alpha^3} - \frac{3\,\kappa^2}{4\alpha^4}, \qquad \frac{\partial B}{\partial \alpha} = -\frac{\sigma\,\kappa\,(T-t)}{\alpha^2} - \frac{\kappa^2\,(T-t)^2}{2\alpha^2} - \frac{\kappa^2\,(T-t)}{\alpha^3}. \tag{C.5}$$

Substituting (C.5)into (C.4) yields

$$\begin{aligned}\frac{\partial V^2}{\partial \alpha} = &\Big(-\frac{\sigma^2}{2\alpha^2} - \frac{2\sigma\kappa}{2\alpha^3} - \frac{3\kappa^2}{4\alpha^4}\Big)(1-M) + 2A\,(T-t)M \\ &+ \Big(\frac{\sigma\kappa\,(T-t)}{\alpha^2} + \frac{\kappa^2\,(T-t)^2}{2\alpha^2} + \frac{\kappa^2\,(T-t)}{\alpha^3}\Big)M + 2B\,(T-t)M.\end{aligned}$$

Since $\frac{\partial V}{\partial \alpha} = \frac{1}{2V}\,\frac{\partial V^2}{\partial \alpha}$ and $\frac{\partial c}{\partial V} = e^{-r\,(T-t)}\,F(t,T)\,\mathscr{N}'(d_1)$, it follows that

$$\begin{aligned}v_c^{\alpha} = e^{-r\,(T-t)}\,F(t,T)\,\mathscr{N}'(d_1)\,\frac{1}{2V}\Big(&\big(-\tfrac{\sigma^2}{2\alpha^2} - \tfrac{2\sigma\kappa}{2\alpha^3} - \tfrac{3\kappa^2}{4\alpha^4}\big)(1-M) \\ &+ \big(\tfrac{\sigma\kappa\,(T-t)}{\alpha^2} + \tfrac{\kappa^2\,(T-t)^2}{2\alpha^2} + \tfrac{\kappa^2\,(T-t)}{\alpha^3}\big)M + 2\,(T-t)M\,(A+B)\Big).\end{aligned}$$

C.3.3 Kappa-Vega (v_c^{κ})

We begin by differentiating V^2 with respect to κ

$$\frac{\partial V^2}{\partial \kappa} = \frac{\partial A}{\partial \kappa}\,(1-M) - \frac{\partial B}{\partial \kappa}M. \tag{C.6}$$

From the definitions of A and B we compute

$$\frac{\partial A}{\partial \kappa} = \frac{\sigma}{2\alpha^2} + \frac{\kappa}{2\alpha^3}, \quad \frac{\partial B}{\partial \kappa} = \frac{\sigma(T-t)}{\alpha} + \frac{\kappa(T-t)^2}{\alpha} + \frac{\kappa(T-t)}{\alpha^2}.$$

Substituting into (C.6) gives

$$\frac{\partial V^2}{\partial \kappa} = \Big(\frac{\sigma}{2\alpha^2} + \frac{\kappa}{2\alpha^3}\Big)(1-M) - \Big(\frac{\sigma(T-t)}{\alpha} + \frac{\kappa(T-t)^2}{\alpha} + \frac{\kappa(T-t)}{\alpha^2}\Big)M.$$

Since $\frac{\partial V}{\partial \kappa} = \frac{1}{2V}\frac{\partial V^2}{\partial \kappa}$, we obtain

$$\frac{\partial V}{\partial \kappa} = \frac{1}{2V}\left(\Big(\frac{\sigma}{2\alpha^2} + \frac{\kappa}{2\alpha^3}\Big)(1-M) - \Big(\frac{\sigma(T-t)}{\alpha} + \frac{\kappa(T-t)^2}{\alpha} + \frac{\kappa(T-t)}{\alpha^2}\Big)M\right).$$

Finally, since $\frac{\partial c}{\partial V} = e^{-r(T-t)}F(t,T)\mathcal{N}'(d_1)$, it follows that

$$\nu_c^{\kappa} = e^{-r(T-t)}F(t,T)\mathcal{N}'(d_1)\frac{1}{2V}\left(\big(\tfrac{\sigma}{2\alpha^2} + \tfrac{\kappa}{2\alpha^3}\big)(1-M) - \big(\tfrac{\sigma(T-t)}{\alpha} + \tfrac{\kappa(T-t)^2}{\alpha} + \tfrac{\kappa(T-t)}{\alpha^2}\big)M\right).$$

C.4 Rho (ρ_c)

We differentiate $c(t)$ with respect to r

$$\rho_c = \frac{\partial}{\partial r}\Big(e^{-r(T-t)}\big(F(t,T)\mathcal{N}(d_1) - K\mathcal{N}(d_2)\big)\Big) = -c(t)(T-t).$$

C.5 Theta (θ_c)

Let $\tau = T-t$. Then

$$\frac{\partial c(t)}{\partial t} = \frac{\partial c(t)}{\partial \tau}\frac{\partial \tau}{\partial t} = \frac{\partial c(t)}{\partial \tau}(-1) = -\frac{\partial c(t)}{\partial \tau}.$$

We differentiate $c(t)$ with respect to t

$$\begin{aligned}\theta_c = \frac{\partial c(t)}{\partial t} &= \frac{\partial}{\partial t}\Big(e^{-r(T-t)}\big(F(t,T)\mathcal{N}(d_1) - K\mathcal{N}(d_2)\big)\Big) \\ &= e^{-r(T-t)}\Big(r\big(F(t,T)\mathcal{N}(d_1) - K\mathcal{N}(d_2)\big) + F(t,T)\mathcal{N}'(d_1)\frac{\partial d_1}{\partial t} - K\mathcal{N}'(d_2)\frac{\partial d_2}{\partial t}\Big).\end{aligned}$$

Using relation (C.1), and

$$\frac{\partial d_2}{\partial t} = \frac{\partial d_1}{\partial t} - \frac{\partial V}{\partial t},$$

one finds

$$\theta_c = e^{-r(T-t)}\Big(r\big(F(t,T)\mathcal{N}(d_1) - K\mathcal{N}(d_2)\big) + K\mathcal{N}'(d_2)\frac{\partial V}{\partial t}\Big).$$

Here

$$\frac{\partial V}{\partial t} = \frac{\partial V^2}{\partial t}\frac{1}{2V} = \frac{1}{2V}\frac{\partial}{\partial t}\Big(A\big(1-M\big) - BM\Big).$$

Note that A is constant with respect to t, hence $\frac{\partial A}{\partial t} = 0$.

$$\frac{\partial M}{\partial t} = \frac{\partial}{\partial t}\big(e^{-2\alpha(T-t)}\big) = 2\alpha\, e^{-2\alpha(T-t)} = 2\alpha M.$$

Next, we have

$$\frac{\partial B}{\partial t} = \frac{\sigma\,\kappa}{\alpha}(-1) + \frac{2\,\kappa^2(T-t)}{2\alpha}(-1) + \frac{\kappa^2}{2\alpha^2}(-1),$$

which simplifies to

$$\frac{\partial B}{\partial t} = -\frac{\sigma\,\kappa}{\alpha} - \frac{\kappa^2(T-t)}{\alpha} - \frac{\kappa^2}{2\alpha^2}.$$

Since

$$\frac{\partial V^2}{\partial t} = -A\frac{\partial M}{\partial t} - \Big(\frac{\partial B}{\partial t}M + B\frac{\partial M}{\partial t}\Big),$$

replacing terms

$$\begin{aligned}\frac{\partial V^2}{\partial t} &= -2\alpha A M - \Big(\big(-\tfrac{\sigma\kappa}{\alpha} - \tfrac{\kappa^2(T-t)}{\alpha} - \tfrac{\kappa^2}{2\alpha^2}\big)M - 2\alpha B M\Big)\\ &= M\Big(-2\alpha A + \frac{\sigma\kappa}{\alpha} + \frac{\kappa^2(T-t)}{\alpha} + \frac{\kappa^2}{2\alpha^2} - 2\alpha B\Big).\end{aligned}$$

After collecting terms one finds by expanding and completing the square

$$\frac{\partial V^2}{\partial t} = -M\big(\sigma + \kappa(T-t)\big)^2.$$

Hence

$$\frac{\partial V}{\partial t} = \frac{M}{2V}\big(\sigma + \kappa(T-t)\big)^2.$$

Substituting into (C.5) and using (C.1), along with the relation $\frac{\partial d_2}{\partial t} = \frac{\partial d_1}{\partial t} - \frac{\partial V}{\partial t}$, we obtain

$$\theta_c = e^{-r(T-t)}\left(r\big(F(t,T)\mathcal{N}(d_1) - K\mathcal{N}(d_2)\big) + K\mathcal{N}'(d_2)\Big(-M\big(\sigma + k(T-t)\big)^2\frac{1}{2V}\Big)\right).$$